



Bifurcation sequence in the wakes of a sphere and a cube

Ricardo A. Schuh Frantz¹ , Chloé Mimeau² , Mikail Salihoglu³ ,
Jean-Christophe Loiseau¹  and Jean-Christophe Robinet¹ 

¹Laboratory DynFluid, Ecole Nationale Supérieure d'Arts et Métiers, Paris, France

²Laboratory M2N, Conservatoire National des Arts et Métiers, Paris, France

³Jean Le Rond d'Alembert Institute, Sorbonne Université, Paris, France

Corresponding author: Ricardo A. Schuh Frantz, rasfrantz@gmail.com

(Received 16 January 2025; revised 7 May 2025; accepted 6 July 2025)

A literature review suggests that the flows past simply connected bodies with aspect ratio close to unity and symmetries aligned with the flow follow a consistent sequence of regimes (steady, periodic, quasiperiodic) as the Reynolds number increases. However, evidence is fragmented, and studies are rarely conducted using comparable numerical or experimental set-ups. This paper investigates the wake dynamics of two canonical bluff bodies with distinct symmetries: a cube (discrete) and a sphere (continuous). Employing three-dimensional (3-D) global linear stability analysis and nonlinear simulations within a unified numerical framework, we identify the bifurcation sequence driving these regime transitions. The sequence: a pitchfork bifurcation breaks spatial symmetry; a Hopf bifurcation introduces temporal periodicity (St_1); a Neimark–Sacker bifurcation destabilises the periodic orbit, leading to quasiperiodic dynamics with two incommensurate frequencies (St_1 , St_2). A Newton–Krylov method computes the unstable steady and periodic base flows without imposing symmetry constraints. Linear stability reveals similarities between the cube and sphere in the spatial structure of the leading eigenvectors and in the eigenvalue trajectories approaching instability. This study provides the first confirmation of a Neimark–Sacker bifurcation to quasiperiodicity in these 3-D wakes, using Floquet stability analysis of computed unstable periodic orbits and their Floquet modes. The quasiperiodic regime is described in space and time by the Floquet modes' effects on the base flow and a spectrum dominated by the two incommensurate frequencies and tones arising from nonlinear interactions. Although demonstrated for a cube and a sphere, this bifurcation sequence, leading from steady state to quasiperiodic dynamics, suggests broader applicability beyond these geometries.

Key words: instability, bifurcation, vortex shedding

1. Introduction

The exploration of viscous fluid interactions with non-streamlined, three-dimensional (3-D) bodies holds critical relevance for fluid dynamicists and engineers due to its diverse practical applications, ranging from medicine and engineering to biology and hydrodynamics. Bluff bodies, such as spheres and cubes, pose inherent challenges due to their large-scale unsteadiness, which can induce increased drag and flow-induced vibrations. Unsteadiness often leads to off-centre forces, complicating manoeuvrability. For example, the persistence of large-scale unsteady coherent structures contributes significantly to the fuel consumption of heavy vehicles such as trucks and buses (Choi, Lee & Park 2014). The study of three-dimensional flow dynamics around canonical bluff bodies aids in understanding transitional behaviour and instability development in these flows, which is crucial for interpreting more complex configurations in the transportation industry.

A defining characteristic of bluff bodies is how the boundary layer separates from the body's surface, causing the flow to detach for a significant portion of the body's length. This detachment results in a larger wake, an incomplete pressure recovery and, consequently, substantially higher drag values compared with streamlined bodies like aerofoils, which are designed to minimise wake by confining flow separation to smaller body sections. The classification of bluff bodies therefore largely depends on their aerodynamic behaviour rather than on their intrinsic physical shape.

The interaction between a solid body and a moving fluid leads to the immediate viscosity-induced formation of a boundary layer on the body surfaces and a resultant pressure drop. Given a constant flow velocity U_∞ and a constant kinematic viscosity ν across a bluff body of characteristic length L , the dimensionless Reynolds number, defined as $Re = U_\infty L / \nu$, plays a major role in determining fluid dynamics. At very low Reynolds numbers, where viscosity dominates, the flow adheres closely to the surfaces of the bluff body. This adherence maintains flow symmetry in all characteristic dimensions, namely streamwise, vertical, spanwise and temporal, resulting in continuous streamlines. As the Reynolds number increases (e.g. $Re > O(1-10)$), convection mechanisms become significant, changing the nature of the flow and allowing recirculation regions to form. To the best of our knowledge, the onset of recirculation zones has not yet been interpreted as a bifurcation, despite the evident loss of symmetry in the streamwise direction. However, this question will not be addressed in this study, which focuses on bifurcations of detached flows. When the Reynolds number is increased, the wake then undergoes successive bifurcations until the emergence of chaotic behaviour, eventually leading to turbulence. Bluff bodies are well-known flow oscillators subject to global instabilities and self-sustaining dynamics. The study of the first bifurcations occurring in bluff-body flows has long been, and still is, a subject of great interest for many geometries.

1.1. Infinite span bluff bodies

The canonical case of flow past a circular cylinder with infinite span has been studied since Bénard and von Kármán in the early 1900s, and has become a benchmark in computational fluid dynamics. After the generation of a steady-state wake for $Re > 6$, the flow past a circular cylinder undergoes a Hopf bifurcation and becomes unstable for $Re > 46.6$ (Jackson 1987; Frantz, Loiseau & Robinet 2023), leading to the development of the von Kármán vortex street and the loss of time invariance. At this point, the flow begins to oscillate with a Strouhal number $St = f D / U_\infty \simeq 0.122$, where f is the vortex shedding frequency.

The flow then experiences a second (subcritical) pitchfork bifurcation at $Re \approx 189$ (Barkley & Henderson 1996; Barkley 2005; Blackburn, Marques & Lopez 2005; Giannetti, Camarri & Luchini 2010; Frantz *et al.* 2023), where the destabilisation

of mode A leads to a three-dimensional transition (loss of spanwise invariance); the streamwise vorticity of mode A shows odd symmetry with respect to the wake centreline (Blackburn & Lopez 2003). The seminal Floquet stability analysis conducted by Barkley & Henderson (1996), and later extended by Blackburn & Lopez (2003), also identified a secondary three-dimensional instability at $Re = 259$ and 256 , respectively, corresponding to the mode B instability and for which the streamwise vorticity shows even symmetry with respect to the wake centreline.

The flow scenario past a square cylinder has been shown to be very similar to that of the circular cylinder by Kelkar & Patankar (1992) and Sohankar, Norberg & Davidson (1998) for the first bifurcation (Hopf) ($Re \approx 51-53$) and by Robichaux, Balachandar & Vanka (1999) for the mode A ($150 < Re < 175$) and mode B ($175 < Re < 205$) instabilities.

1.2. Finite span bluff bodies

In the present study, we use the finite span bluff body to refer to a body with a finite span and thus a finite aspect ratio AR (which will later be defined as compact), such as a sphere or cube, as opposed to infinite-span bodies such as the circular or square cylinder. Although less extensive than its infinite span counterpart for the circular- and square-cylinder cases, the literature on flows around finite span bluff bodies is informative and includes experimental, theoretical and numerical works, highlighting similarities and differences relative to their infinite span counterparts. A survey of the relevant literature is presented here, with the support of [Appendix A](#) which provides a visual summary and comparison across different bluff-body flows. In the Appendix, as well as in the following subsections, we intentionally adhere to the original terminology used in the referenced literature to describe the temporal dynamics and spatial symmetries. In particular, the names, the nature and characteristics of the flow bifurcations are faithfully presented as reported, without reinterpretation or modification. Concerning symmetries, ‘reflectional symmetry’ (invariance under reflection across a plane) and ‘planar symmetry’ (symmetry about the midplane) are used interchangeably.

1.2.1. Sphere

Flow studies on a sphere (solid and fixed) can be traced back to the experiments of Taneda (1956) and others (Achenbach 1974; Nakamura 1976; Sakamoto & Haniu 1995; Schouveiler & Provansal 2002), through theoretical works (Chester, Breach & Proudman 1969; Sano 1981), numerical simulations (Johnson & Patel 1999; Mittal 1999; Ghidersa & Dušek 2000; Tomboulides & Orszag 2000; Thompson, Leweke & Provansal 2001; Constantinescu & Squires 2004), and linear stability analyses in both the incompressible (Bouchet, Mebarek & Dušek 2006; Pier 2008; Meliga *et al.* 2009b; Citro *et al.* 2017) and compressible regimes (Sansica *et al.* 2018, 2020). Using the diameter of the sphere to express the Reynolds number, steady-state axisymmetric flow is found for $Re \lesssim 200$ (regime I), while steady-state planar symmetric flow persists up to $Re \lesssim 270$ (regime II) before time-periodic dynamics sets in, characterised by periodic vortex shedding, while preserving the wake’s planar symmetry (regime III). In agreement with the critical Reynolds numbers Re_c at which the changes in flow regimes are observed in all the above-mentioned references, the stability analyses carried out by Meliga *et al.* (2009b) and Citro *et al.* (2017) identify the first two bifurcations of flow past a solid sphere: a first destabilisation occurs for a stationary mode via a supercritical pitchfork bifurcation at $Re_{c,1} = 212.6$ (Meliga *et al.* 2009b), $Re_{c,1} = 212.4$ (Citro *et al.* 2017) followed by a second destabilisation for an oscillating mode through a supercritical Hopf bifurcation at $Re_{c,2} = 280.7$ (Meliga *et al.* 2009b), $Re_{c,2} = 271.8$ (Citro *et al.* 2017).

Experiments of Sakamoto & Haniu (1990), Chrust, Goujon-Durand & Wesfreid (2013) and the direct numerical simulation (DNS) studies of Kalro & Tezduyar (1998), Mittal (1999), Mittal & Najjar (1999), Lee (2000), Tomboulides & Orszag (2000), Bouchet *et al.* (2006) report that, when increasing Re , the time-periodic dynamics of flow past a sphere is followed by a new regime (IV) characterised by an ‘irregular shedding’ of the vortical structures, associated with the measurement of two frequencies in the wake: St_1 (the shedding frequency, close to the one identified after the onset of the Hopf bifurcation) and a lower frequency St_2 . Based on the collective evidence from all references, this regime transition is observed in a range $350 < Re_{c,3} < 480$. Spatially, this new regime (IV) is also associated in the literature with the loss of the planar symmetry. Actually, this question of planar symmetry breaking will be particularly addressed and revisited in the present paper. Finally, in what could be interpreted as a fifth regime, Sakamoto & Haniu (1990) and Chrust *et al.* (2013) respectively reveal that at $Re > 480$ and $Re = 430$, the vortex shedding direction oscillates intermittently from left to right and that the shedding plane undergoes a periodic rotation about the downstream surface of the sphere. In the particular case of a rotating rigid sphere, Sierra-Ausín *et al.* (2022) found a ‘quasiperiodic’ state. Refer to the line ‘Sphere’ in table 3 of Appendix A for a summary of the first regimes and bifurcations of flow past a sphere.

1.2.2. Flat and thick circular disks

Natarajan & Acrivos (1993), Kiya, Ishikawa & Sakamoto (2001) and Fabre, Auguste & Magnaudet (2008) studied the similarities and differences between the flow past a sphere and the flow past a very thin ($AR \ll 1$), almost flat, circular disk placed perpendicularly to the main flow direction. Despite the discrepancy in the threshold for the change in regime (respectively $Re_{c,1} = 212$ and $Re_{c,1} = 115$ for the sphere and the flat disk), both bluff bodies experience the sequence of a pitchfork followed by a Hopf bifurcation (at $Re_{c,2} = 121 - 123$ for the flat disk). Considering a very thin disk with $AR = 1/10$, Shenoy & Kleinstreuer (2008) observed an ‘irregular motion of the vortex shedding’ accompanied by a loss of planar symmetry in the wake at $Re_c = 280$. At $Re = 300$, they measured two distinct frequencies, $St_1 = 0.122$ and $St_2 = 0.041$. The authors relate the low frequency St_2 to the irregular motion of the vortex shedding location and to the ‘pumping motion’ of the recirculation zone. This sequence of regimes follows that reported for the sphere. However, in contrast to the sphere case, the Hopf bifurcation (i.e. the second bifurcation) in the flow past a flat disk is followed by the loss of the reflectional symmetry. DNS by Fabre *et al.* (2008) and stability analysis performed by Meliga *et al.* (2009a) additionally report another bifurcation on the flow past a flat disk at $Re_c = 140$ and $Re_c = 143.7$, respectively, making the flow switch from an RSB (reflectional symmetry breaking) to an RSR (reflectional symmetry recovering) regime where the previously lost planar symmetry is retrieved. According to the weakly nonlinear analysis of Meliga *et al.* (2009a), the condition for this bifurcation to occur is that the development of the standing wave must re-stabilise the stationary eigenmode. This (sub)bifurcation, characterised by the recovery of the lost reflectional symmetry, and occurring between the Hopf bifurcation and the onset of a second low frequency St_2 , was also observed by Kim & Choi (2003) in flow past a hemisphere (where half of a sphere faces upstream and its flat surface faces downstream). This phenomenon of symmetry recovery, as observed in the case of a flat disk and a hemisphere, remains poorly understood (see the lines ‘Flat disk ($AR \ll 1$)’ and ‘Hemisphere’ in table 3).

Concerning flow past a thick circular disk (also placed perpendicularly to the flow direction), the DNS studies performed by Auguste, Fabre & Magnaudet (2010) for a thick disk of $AR = 1/3$ and by Pierson *et al.* (2019) for a thick disk of $AR = 1$ show that the flow experiences the following sequence of bifurcations: a steady (pitchfork) bifurcation

($Re_{c,1} = 159.4$ for $AR = 1/3$ and $Re_{c,1} = 276$ for $AR = 1$), a Hopf bifurcation leading to the time-periodic shedding of the planar symmetric wake ($Re_{c,2} = 179.8$ for $AR = 1/3$ and $Re_{c,2} = 355$ for $AR = 1$) and finally a third bifurcation ($Re_{c,3} = 184\text{--}185$ for $AR = 1/3$ and $Re_{c,3} = 395$ for $AR = 1$) leading to the occurrence of a secondary frequency, which breaks the wake's reflectional symmetry for $AR = 1/3$ but preserves it for $AR = 1$ (see the 'Thick disk lines' in [table 3](#)).

1.2.3. Finite-span cylinder

Yang, Feng & Zhang (2022) performed direct simulations and global stability analysis of the flow past a finite-span cylinder with two free flat ends, considering geometries with different aspect ratios. For unity aspect ratio ($AR = 1$), the authors describe a sequence of bifurcations with, first, a loss of spatial symmetry of the recirculation zone at $Re_{c,1} = 172.2$ via a supercritical regular (i.e. pitchfork) bifurcation, then periodic unsteadiness through a Hopf bifurcation at $Re_{c,2} = 282$ and finally a 'more chaotic' flow from $Re_{c,3} \approx 332$ characterised by the onset of a new lower frequency St_2 , extracted from the power spectral density (PSD) of the spanwise lift coefficient. It is interesting to note that the DNS and the linear stability analysis performed by Yang *et al.* (2022) for the flow past a small cylinder of $AR = 1.75$ could not identify a pitchfork bifurcation. The authors explain that for $AR \gtrsim 1.75$, the flow never experiences the steady-planar symmetric wake and directly transitions from the steady-axisymmetric regime to the periodic shedding of planar symmetric hairpin vortices (like in the cylinder case), as reported in § 1.1. This primary Hopf bifurcation is then followed by the transition identified by the appearance of the new lower frequency St_2 (see the lines 'Small cylinder' and 'Infinite span cylinder' in [table 3](#) for a summary).

1.2.4. Cube

When numerically investigating the flow past a solid cube, Saha (2004, 2006) and Khan *et al.* (2020b) show that the transition sequence and flow structures closely match those of a sphere. The first spatial and steady bifurcation occurs at $200 < Re_{c,1} < 215$, transforming the orthogonally symmetric flow into a planar symmetric one, and a second temporal (Hopf) bifurcation occurs at $250 < Re_{c,2} < 276$, maintaining the planar symmetry. Despite a change in critical values ($Re_{c,1} = 186$ and $Re_{c,2} = 285$), these predictions were clearly confirmed by the experiments of Klotz *et al.* (2014). More recently, the numerical study of Meng *et al.* (2021) detailed the different regimes in the wake transition behind a cube, confirming previous observations: First, a steady-symmetric regime (I) in which the steady orthogonal symmetric wake transitions to a steady planar symmetry wake (II) at $Re_{c,1} \approx 207$. Second, an alternating detachment of streamwise vortex tubes arises due to a supercritical Hopf bifurcation at $Re_{c,2} \approx 252$, leading to a hairpin vortex shedding regime. Then, this single-frequency hairpin vortex shedding (regime III) is followed by a 'quasiperiodic vortex shedding' (regime IV) arising at $Re_{c,3} \approx 281$ with a 'limit torus' composed of 'incommensurate' ($St_1/St_2 \notin \mathbb{Q}$) frequencies $St_1 \approx 0.0982$ and $St_2 \approx 0.0281$, while preserving the planar symmetry (see the line 'Cube' in [table 3](#) for a summary).

1.2.5. Polyhedron and ellipsoidal bodies

Torlak *et al.* (2019) analysed the low-Reynolds-number flow around polyhedron-shaped bodies, specifically focusing on the cube, octahedron and dodecahedron. Despite not presenting estimates of the regime thresholds, the figures indicate a loss of spatial symmetry followed by a loss of temporal symmetry. Similar conclusions were also found in the wake of ellipsoidal particle shapes (Richter & Nikrityuk 2012).

1.2.6. Industrial-type bluff bodies

Concerning industrial applications of bluff bodies, one example is the flow past an Ahmed body (Ahmed, Ramm & Falin 1984), a prototypical simplification of a passenger-car geometry. In the low Reynolds regime, the experimental works of Grandemange, Cadot & Gohlke (2012) report a steady planar-symmetric state (indeed, the presence of the ground induces a top-bottom asymmetry of the wake from the first regime) until the wake loses this planar symmetry (while remaining steady) via a pitchfork bifurcation at $Re_{c,1} = 340$. Then, a Hopf bifurcation leads to unsteadiness at $Re_{c,2} = 410$ (see the line ‘Ahmed body’ in table 3). As another industrial-type example, one can mention the case of a blunt-based bluff body. The numerical work of Rigas, Esclapez & Magri (2017) investigated such non-canonical geometry with $AR \approx 6$, using a combination of direct simulations and stability analyses. They revealed that a first pitchfork bifurcation at $Re_{c,1} = 424$ destabilises a steady mode that breaks the axisymmetry of the wake. A steady reflectional symmetry is preserved up to $Re_{c,2} = 605$ when an eigenmode becomes unstable due to a Hopf bifurcation, leading to a periodic regime of vortex shedding. An aperiodic, ‘presumably quasiperiodic’, dynamics is reported for $675 \leq Re_{c,3} \leq 800$ with two ‘incommensurate frequencies’ ($St_1 = 0.113$ and $St_2 = 0.027$ at $Re = 800$) and multiple other frequencies in the PSD of the centre of pressure. During this presumably quasiperiodic regime, the flow still maintains planar-symmetry while chaotic dynamics is observed for $Re > 900$. Experimental and numerical studies were also performed by Bohorquez *et al.* (2011) for blunt-based bluff bodies with different aspect ratios, in particular, with $AR = 1$ and $AR = 2$. In both cases, they highlight the exact same sequence of regimes as for the $AR = 6$ geometry. (See the lines ‘Blunt-based bluff body’ in table 3 for a summary.)

1.3. Sequence of wake bifurcations

As the Reynolds number increases beyond single digits, a recirculation zone develops behind bluff bodies, gradually extending in length. This zone, whose shape and size depend on the body’s geometry, plays a crucial role in determining the flow dynamics. In the case of infinite span geometries such as flat plates, circular cylinders, square cylinders or axial (or transverse) cylinders with relatively large aspect ratios, the initial bifurcation encountered is a Hopf bifurcation. This primary bifurcation transitions the wake from a two-dimensional (2-D) steady state to a two-dimensional time-periodic (unsteady) state. It is important to note that the transition to three-dimensional flow characteristics is observed only during subsequent secondary bifurcations, through the loss of spanwise invariance, a phenomenon well-documented by Barkley & Henderson (1996).

Conversely, for finite span bluff body geometries with small aspect ratios ($AR \lesssim 2$), which are the focus of this study, the first bifurcation differs because the wake is three-dimensional from the initial steady regime; unsteadiness then arises via a Hopf bifurcation, which constitutes the second bifurcation in this sequence. Refer to the detailed works of Marquet & Larsson (2015), Yang *et al.* (2022) and Chiarini & Boujo (2025) for numerical studies on the linear destabilisation of three-dimensional steady wakes and the transition towards two-dimensional behaviour when increasing the aspect ratio of a flat plate, a circular cylinder and rectangular prisms, respectively. In particular, Chiarini & Boujo (2025) studied the first bifurcations of flow past rectangular prisms by varying body elongation in the spanwise or streamwise direction. They report changes in the nature of the primary pitchfork bifurcation, observing subcritical and codimension-2 bifurcations, and even its complete replacement by a supercritical Hopf bifurcation for higher width-to-height ratio.

In this work, we focus on finite span bluff bodies with the following characteristics: static, rigid, simply connected bodies with aspect ratio close to unity and symmetries aligned with the main flow direction, simply referred to as compact-simplyconnected bluff bodies (CSC-BB) for conciseness. Therefore, we do not consider bodies without symmetries aligned with the flow direction or non-simply connected bodies (e.g. Sheard, Thompson & Hourigan 2003). Our comprehensive literature review reveals that the CSC-BB class follows a ubiquitous sequence of flow regimes. More precisely, this pattern involves a sequential breaking of spatio-temporal symmetries that is consistent across various geometries, including both axisymmetric bodies (e.g. spheres, flat disks, thick disks, short cylinders) and bodies with reflectional symmetries (e.g. hemispheres, cubes, Ahmed bodies, short flat plates). The first two bifurcations, namely a ‘supercritical pitchfork’ followed by a ‘supercritical Hopf’, have already been clearly identified in the literature for most canonical CSC-BB shapes (see [table 3](#)). However, despite the large number of existing studies, to the knowledge of the authors, there is no explicit characterisation of the bifurcations following the pitchfork and Hopf bifurcations. As reported in our survey, after the unsteady time-periodic regime (III) triggered by the Hopf bifurcation, different papers identified a fourth regime (IV). During this IVth regime, the references observe two frequencies; some mention a ‘lower’ frequency qualitatively, while others provide its quantitative value, and very few papers explicitly mention the words ‘incommensurate’ when comparing the two frequencies or ‘quasiperiodic’ to describe the regime associated with this two-frequency oscillation (see Meng *et al.* 2021 (cube case) and Rigas *et al.* 2017 (blunt-based bluff body)). This change in flow dynamics strongly suggests a third bifurcation responsible for the emergence of quasiperiodic dynamics (regime IV) after single-frequency periodicity (regime III). According to dynamical systems theory, for a periodic system to transition to quasiperiodic dynamics (associated with the observation of two frequencies), a so-called Neimark–Sacker bifurcation is needed (Neimark 1959, Sacker 1964, Arnold 2012). This bifurcation is analogous to the Hopf bifurcation of a fixed point for periodic orbits, and is thus often referred to as a secondary Hopf bifurcation.

Consequently, we can confidently extrapolate that CSC-BBs undergo the following sequence of bifurcations:

(I) pitchfork; (II) Hopf; and (III) Neimark–Sacker.

To support our conjectured sequence, this paper employs global linear stability analysis of the wake of two canonical bluff-body flows: a cube and a sphere. These two geometries cover the range of symmetry conditions from discrete (cube) to continuous (sphere). The discrete symmetry stands for reflectional symmetry (i.e. invariance under reflection across a specific plane), while continuous symmetry refers to axisymmetry (i.e. invariance under rotation around a specific axis). As canonical examples of CSC-BBs, the cube and the sphere provide well-defined baseline configurations for testing the generality of the bifurcation sequence and for exploring how differences in surface curvature and symmetry properties might influence the onset of successive instabilities.

The paper is structured as follows. In § 2, we outline the overall methodology, including the problem definition, the computational set-up and the global linear stability methodology. Sections 3 and 4 detail the global linear stability analyses conducted to identify respectively the primary (pitchfork) and secondary (Hopf) bifurcations for both cube and sphere geometries. Then, § 5 focuses on the Floquet analysis performed to identify the tertiary bifurcation (Neimark–Sacker) in the three-dimensional flows around the cube and sphere, and § 6 presents a detailed analysis of the quasiperiodic regime using nonlinear simulations. Conclusions and future perspectives are presented in § 7.

2. Numerical methodology

2.1. Governing equations

The flow is modelled using the three-dimensional, incompressible Navier–Stokes equations, expressed in non-dimensional form. These equations describe the evolution of the velocity field $\mathbf{u} = (u, v, w)$ and the pressure field p in the spatial coordinates $\mathbf{x} = (x, y, z)$, corresponding to the streamwise, vertical and spanwise directions, respectively:

$$\nabla \cdot \mathbf{u} = 0 \quad \text{in } \Omega, \quad (2.1a)$$

$$\frac{\partial \mathbf{u}}{\partial t} + (\mathbf{u} \cdot \nabla) \mathbf{u} = -\nabla p + \frac{1}{Re} \nabla^2 \mathbf{u} \quad \text{in } \Omega. \quad (2.1b)$$

Here, Ω represents the computational domain and $Re = U_\infty D / \nu$ is the Reynolds number, our sole control parameter. It is defined using the characteristic length D of the bluff body (that is, the side length for the cube and the diameter for the sphere), the velocity of the free flow U_∞ and the fluid kinematic viscosity ν . The equations are non-dimensionalised using D as the length scale, U_∞ as the velocity scale and D / U_∞ as the time scale.

2.2. Computational domain and boundary conditions

In our simulations, the bluff bodies under consideration, namely the cube and the sphere, are centrally positioned within the computational domain Ω and have a characteristic length $D = 1$. The computational domain is defined by dimensions of (In, Out, Sides) = $(10D, 50D, 10D)$, which means that the bluff body is located $10D$ downstream from the inlet and $50D$ upstream from the outlet, with side boundaries $10D$ away from the centre of the body in both vertical (y) and spanwise (z) directions. These domain dimensions are chosen to balance accuracy and computational cost, while ensuring minimal influence of domain boundaries on the wake dynamics. This set-up aligns with or improves on previous reference studies, as discussed in [Appendix B.1](#). By using the same domain size for both the cube and the sphere, we maintain a consistent numerical environment, facilitating direct comparisons of the flow dynamics between these two canonical bluff-body shapes and also isolating the influence of body geometry on the wake dynamics and transition phenomena.

We enforce a Dirichlet boundary condition with a uniform velocity field $\mathbf{u} = (U_\infty, 0, 0) = (1, 0, 0)$, assuming steady freestream flow at the inlet. At the outlet, we prescribe an open boundary condition with zero normal pressure gradient (Neumann condition), allowing the flow to exit the domain without artificial reflections. A no-slip condition is imposed on the body surface to model fluid–solid interactions. Free-slip boundary conditions are imposed on all side boundaries (upper, lower and lateral), allowing the use of a coarser mesh in regions far from the body, where high resolution is not required. [Figure 1](#) provides a detailed illustration of the computational domain, including spatial configurations and boundary conditions.

2.3. Numerical approach and discretisation

Direct numerical simulation (DNS) studies are performed using Nek5000, an efficient open-source spectral-element code for fluid dynamics (Fischer *et al.* 2008). It combines the flexibility of finite elements with the fast convergence of spectral methods. The computational domain, Ω , is divided into E non-overlapping hexahedral elements, $\Omega = \bigcup_{i=1}^E \Omega_i$, allowing for local mesh refinement and efficient parallelisation. Within each element, high-order tensor-product Legendre polynomial bases of degree N are employed, defined at Gauss–Lobatto–Legendre quadrature points, while the pressure is approximated using discontinuous polynomials of degree $N - 2$ at Gauss–Legendre points.

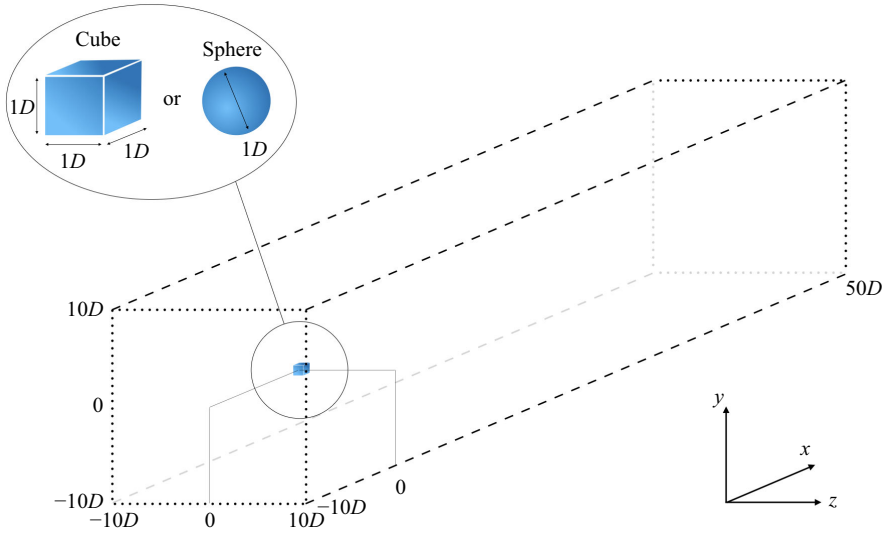


Figure 1. Schematic representation of the computational domain for flow past a cube or sphere. The cube or sphere is centrally positioned within the domain. Dashed lines indicate symmetry boundaries, while dotted lines represent open boundary conditions at the inlet and outlet.

This staggered arrangement ensures compatibility between the velocity and pressure spaces, enhancing numerical stability and enforcing the incompressibility condition discretely. In this study, we use $N = 7$ for the velocity basis.

For the cube simulations, the mesh used in this study contains 49 176 elements, maintaining symmetry in the vertical (y) and spanwise (z) directions, and the sphere simulations involve a mesh with 63 281 elements that accurately capture the sphere's curvature. This results in approximately 25 million and 32 million degrees of freedom for the cube and the sphere meshes, respectively. These high-resolution meshes ensure that geometric features and flow characteristics are accurately resolved. For details on mesh sensitivity and spatial discretisation choices, see [Appendix B.2](#).

Temporal discretisation is performed using a semi-implicit scheme. The viscous and pressure terms are handled implicitly with a third-order backward differentiation formula to ensure stability, while the nonlinear convective term is treated explicitly using third-order extrapolation. The time step is dynamically adjusted to maintain a target Courant number, $Co < 0.5$, satisfying the Courant–Friedrichs–Lewy (CFL) condition.

To remove potential spurious numerical artefacts associated with nonlinear terms, we employ a combination of dealiasing and explicit filtering. Dealiasing employs a higher-order quadrature for the nonlinear convective term, minimising aliasing errors that can lead to spurious energy growth at high wavenumbers (Orszag 1971). Explicit filtering, applied after each time step, selectively damps high-order modes akin to hyperviscosity, further enhancing stability without impacting resolved scales (Fischer & Mullen 2001).

2.4. Linear stability analysis

We characterise the stability of flows around a bluff body at various Re using global linear stability analysis, which assesses the evolution of small perturbations to a base flow, and predicts the onset of instabilities and bifurcations. The base flow, computed from the Navier–Stokes equations (2.1), is either a steady state (fixed point), $\mathbf{Q} = (\mathbf{U}, P)^T$, or a time-periodic solution (periodic orbit), $\mathbf{Q}(t) = (\mathbf{U}(t), P(t))^T$. We employ a

matrix-free, time-stepping approach based on Krylov methods – specifically the Krylov–Schur algorithm (Stewart 2001) – to solve large-scale eigenvalue problems. This method supports both types of base flows, enabling a comprehensive stability analysis of fully three-dimensional configurations.

We superimpose infinitesimal perturbations $\mathbf{q}(\mathbf{x}, t) = (\mathbf{u}, p)^T$ onto \mathbf{Q} :

$$\mathbf{Q} + \varepsilon \mathbf{q} = (\mathbf{U} + \varepsilon \mathbf{u}, P + \varepsilon p)^T, \quad \text{with } \varepsilon \ll 1. \quad (2.2)$$

This applies to steady states and extends to periodic cases, $\mathbf{Q}(t) + \varepsilon, \mathbf{q}(t)$, as is covered in § 2.4.2. Substituting (2.2) into the evolution operator and linearising with respect to ε yields the linearised Navier–Stokes equations (LNSEs):

$$\nabla \cdot \mathbf{u} = 0 \quad \text{in } \Omega, \quad (2.3a)$$

$$\frac{\partial \mathbf{u}}{\partial t} + (\mathbf{u} \cdot \nabla) \mathbf{U} + (\mathbf{U} \cdot \nabla) \mathbf{u} = -\nabla p + \frac{1}{Re} \nabla^2 \mathbf{u}, \quad \text{in } \Omega, \quad (2.3b)$$

where \mathbf{u} is the velocity perturbation and p the pressure perturbation. The LNSE can be further compactly represented in matrix form as

$$\mathcal{B} \frac{\partial \mathbf{q}}{\partial t} = \mathcal{L} \mathbf{q}, \quad (2.4)$$

where $\mathcal{B} = ((\mathbf{I}, 0), (\mathbf{0}, 0))^T$ is the (singular) mass matrix due to incompressibility and \mathcal{L} is the Jacobian matrix. Assuming a normal mode decomposition via a Laplace transform in time, the infinitesimal perturbation has the form

$$\mathbf{q}(\mathbf{x}, t) = \hat{\mathbf{q}}(\mathbf{x}) e^{\lambda t} + \text{c.c.}, \quad (2.5)$$

where $\hat{\mathbf{q}}(\mathbf{x})$ is the spatial eigenfunction of the perturbation, dependent on all three spatial coordinates $\mathbf{x} = (x, y, z)$, and λ is the complex eigenvalue of the considered normal mode. Substituting (2.5) into (2.4) and neglecting higher-order terms yields the generalised eigenvalue problem:

$$\lambda \mathcal{B} \hat{\mathbf{q}} = \mathcal{L} \hat{\mathbf{q}}, \quad (2.6)$$

where the complex eigenvalue $\lambda = \sigma + i\omega$ governs the temporal behaviour of the perturbation. The real part, σ , represents the growth rate, dictating whether perturbations amplify ($\sigma > 0$) or decay ($\sigma < 0$), while the imaginary part, $\omega = 2\pi f$, corresponds to the frequency f . A base flow \mathbf{U} is deemed globally unstable if the eigenvalue problem (2.6) admits at least one solution with a positive growth rate. The corresponding eigenmode, $\hat{\mathbf{q}}(\mathbf{x})$, termed a global eigenmode, represents the spatial structure of the instability throughout the domain. The emergence of global eigenmodes requires that at least one area of the flow exhibits a synchronised, self-sustained oscillation described by a global eigenfunction (Chomaz, Huerre & Redekopp 1988). In the opposite case, where all eigenvalues have negative growth rates, the base flow is globally stable (not temporally self-sustained).

The next two subsections address solving eigenvalue problem (2.6) for steady-state (fixed point) and time-periodic (periodic orbit) base flows.

2.4.1. Fixed points

To solve the problem (2.6), building and storing the Jacobian matrix \mathcal{L} is computationally impractical due to the large number of degrees of freedom in three-dimensional simulations. Instead, we employ a time-stepping approach, based on Krylov methods, that leverages the linearity of the problem and computes the action of the Jacobian over time. We approximate the action of the Jacobian \mathcal{L} via the matrix exponential of the

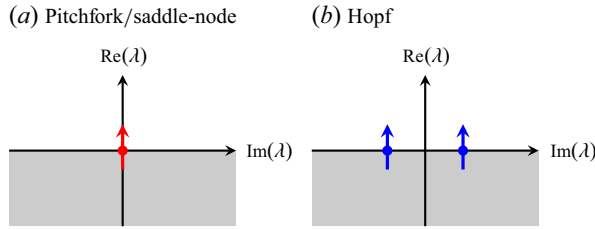


Figure 2. Schematic of bifurcations experienced by a steady-state solution (i.e. fixed point). This diagram illustrates the two types of bifurcations that occur in steady-state flows as a parameter (e.g. Reynolds number) is varied. The shaded region indicates the stable part of the spectrum, i.e. the lower complex half-plane $Re\{\lambda\} = \sigma < 0$. Adapted from Frantz *et al.* (2023).

operator $\mathbf{M}_\tau = e^{\mathcal{L}\tau}$ over a finite sampling time τ . This leads to the large-scale eigenvalue problem:

$$\mathbf{M}_\tau \hat{\mathbf{q}} = \mu \hat{\mathbf{q}}, \quad (2.7)$$

where μ are the eigenvalues of \mathbf{M}_τ , and $\hat{\mathbf{q}}$ are the corresponding eigenmodes. The eigenvalues of \mathcal{L} are then recovered with the natural logarithm transformation $\lambda = \ln(\mu)/\tau$.

Figure 2 illustrates common eigenspectrum structures and how the leading eigenvalue governs the bifurcation type. If the leading eigenvalue crosses the imaginary axis ($\sigma > 0$) with zero imaginary part ($\omega = 0$) and symmetry breaking occurs, the system undergoes a pitchfork bifurcation (figure 2a), resulting in a steady-state solution. If the leading eigenvalue crosses into the unstable half-plane with $\omega \neq 0$, an Hopf bifurcation occurs (figure 2b), leading to periodic dynamics (periodic orbits). To efficiently solve (2.7), we use the NekStab toolbox, which integrates the highly parallel time-stepping capabilities of Nek5000 with Krylov methods. The effectiveness of this methodology in fixed point cases has been demonstrated in several studies (Loiseau *et al.* 2014; Bucci *et al.* 2018; Picella *et al.* 2018; Loiseau *et al.* 2019; Bucci *et al.* 2021).

2.4.2. Periodic orbits

Now, we assess the stability of a periodic orbit $\mathbf{Q}(t) = (\mathbf{U}(t), P(t))^T$ by performing a Floquet analysis. This method, designed for time-periodic systems, evaluates the net effect of small perturbations over one full period τ , determining whether they grow or decay. This evolution is captured by the monodromy matrix \mathbf{M}_τ , which encapsulates the cumulative effect of the linearised dynamics over the period τ . In practice, it is obtained by integrating the linearised system:

$$\mathbf{M}_\tau = \int_0^\tau \mathcal{L}(t) dt, \quad (2.8)$$

where \mathcal{L} is the linearised Jacobian operator around the periodic base flow $\mathbf{Q}(t)$ from which we can assess how perturbations behave over successive periods. The eigenvalue problem to solve therefore writes

$$\mathbf{M}_\tau \hat{\mathbf{q}} = \mu \hat{\mathbf{q}}, \quad (2.9)$$

where $\hat{\mathbf{q}}$ denote the Floquet modes (i.e. the eigenvectors of the monodromy matrix \mathbf{M}_τ) and μ are the corresponding Floquet multipliers (i.e. eigenvalues). The magnitude of the Floquet multipliers indicates the stability of the periodic orbit: if $|\mu| < 1$ for all μ in the spectrum of \mathbf{M}_τ , perturbations decay over one period and the periodic orbit is stable to small disturbances; if there exists at least one eigenvalue μ such that $|\mu| > 1$, perturbations

(a) Pitchfork/saddle-node

(b) Period-doubling/Flip

(c) Neimark–Sacker/secondary-Hopf

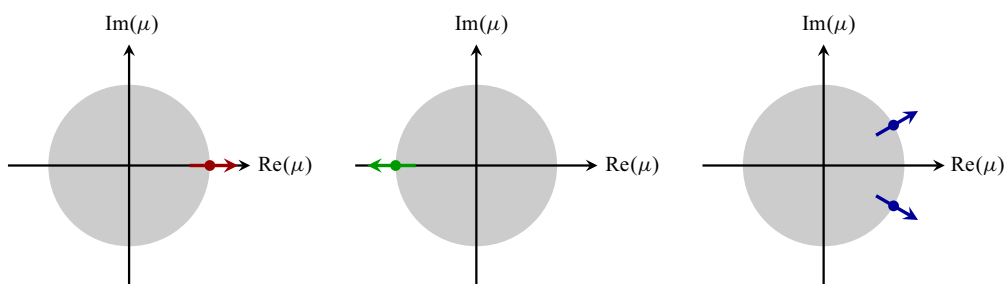


Figure 3. Schematic of bifurcations experienced by a time-periodic base flow (or periodic orbit). This figure depicts three typical bifurcation types in time-periodic systems. The shaded region indicates the stable part of the spectrum, i.e. the unit disk $|\mu| = 1$. Adapted from Frantz *et al.* (2023).

grow over one period, indicating that the periodic orbit is unstable. The Floquet multiplier μ is related to the Floquet exponent λ by $\mu = e^{\lambda\tau}$, where $\lambda = \sigma + i\omega$ is a complex number. Here, σ represents the average growth rate per orbital period (real part) and ω corresponds to an additional frequency component introduced by the perturbation (imaginary part).

Figure 3 illustrates common scenarios of how the leading Floquet multiplier governs the type of bifurcation that the system may undergo.

- (i) Pitchfork bifurcation (figure 3a) ($|\mu| > 1$ and $\mu \in \mathbb{R}^+$): new periodic solutions with different amplitudes or phases emerge from the original orbit. This type of bifurcation often occurs in systems with certain symmetries and can lead to multiple stable periodic solutions coexisting.
- (ii) Period-doubling bifurcation (figure 3b) ($|\mu| > 1$ and $\mu \in \mathbb{R}^-$): a period-doubling or flip bifurcation occurs. Here, the Floquet multiplier moves through $\mu = -1$, indicating that perturbations change sign every period. A new periodic solution with twice the period of the original orbit emerges.
- (iii) Neimark–Sacker bifurcation (figure 3c) ($|\mu| > 1$ and $\mu \in \mathbb{C}$ with a non-zero imaginary part): a pair of complex conjugate Floquet multipliers move across the unit circle, introducing a new frequency into the system. This bifurcation is thus also known as a secondary Hopf bifurcation. The resulting motion is quasiperiodic, characterised by oscillations with two incommensurate frequencies.

As in the fixed point methodology, we employ the matrix-free approach to circumvent the computational impracticability of constructing the monodromy matrix \mathbf{M}_τ . Instead of forming \mathbf{M}_τ explicitly, we compute its action on perturbation vectors by integrating the linearised system over one period τ . Again, we employ the NekStab toolbox, which uses Krylov methods to compute dominant Floquet multipliers and corresponding modes, enabling the stability assessment of periodic orbits in large-scale three-dimensional flows; for a comprehensive overview of Floquet analysis and its applications, we refer the reader to the review by Frantz *et al.* (2023).

2.4.3. Numerical parameters

For the stability analysis of fixed points, the time-stepping approach is based on an integration sampling period equal to $\tau = 1.25$. This value is determined by the product of the number of iterations (n) required by the linear solver (i.e. (2.3)), and the time step (dt) used in both cube and sphere simulations ($\tau = n \times dt$). This choice follows

the recommendations of Frantz *et al.* (2023), which enables the efficient execution of the eigenproblem within a single supercomputer run. For the Floquet analysis involving periodic orbits, τ is set to precisely match the period of the orbit, whose evaluation is described in [Appendix D.2](#). Despite the large domain size, sponge regions were used at the inlet (one element) and outlet (five elements) to minimise potential boundary reflections, acting to gradually zero perturbations, in line with best practices for stability analysis. For the eigenvalue computations, a Krylov basis of size $m = 100$ was employed, with convergence achieved when at least 20 eigenvalues reached an absolute residual of 10^{-6} , while absolute tolerances of 10^{-10} were employed for the velocity and pressure solvers.

2.5. Base flow computation

Steady \mathbf{Q} and periodic $\mathbf{Q}(t)$ base flows are computed using the Jacobian-free Newton–Krylov method, implemented within the open-source NekStab toolbox for Nek5000. [Appendix D](#) details the computation of fixed points and the stabilisation of unstable periodic orbits (UPOs). A generalised minimal residual (GMRES) algorithm is used to solve the linear systems arising in both the fixed point and UPO algorithms. For UPOs, the Newton method is extended to simultaneously compute the exact period τ (see [Appendix D.2](#)). Solver tolerances (for both velocity and pressure) and stopping criteria are dynamically adjusted and bounded by the current residual estimate, ensuring that the solver seeks corrections one order of magnitude smaller than the current residual. This approach enables inexact steps during early iterations – reducing computational costs – while progressively tightening convergence as the residual decreases. Specifically, all base flows are computed until the absolute residual falls below an absolute tolerance of 10^{-10} . Further details on the Newton–GMRES method can be found from Frantz *et al.* (2023).

In §§ 3, 4 and 5, we present the identification of the primary, secondary and tertiary bifurcations for both cube and sphere geometries, based on the global linear stability methodology outlined previously.

3. Primary bifurcation

Cube. From nonlinear simulations, Meng *et al.* (2021) identified a primary bifurcation in the flow past a static cube at a critical Reynolds number $Re_{c,1} \approx 207$. Our investigation, which started with a DNS at $Re = 200$, confirmed the steady state of the flow and revealed, as reported by Meng *et al.* (2021), an orthogonally symmetric recirculation zone directly behind the cube.

Using the Newton–Krylov solver described in [Appendix D.1](#), we meticulously traced the evolution of the orthogonally symmetric flow solution from $Re = 200$ to $Re = 212$. This process unveiled a transition to an unstable base flow at $Re = 207$, perfectly orthogonally symmetric, as depicted in perpendicular cross-sections ($z = 0$, $y = 0$, $x = 0$) in [figure 4\(a,c,e\)](#). It is crucial to note that our analysis did not impose additional symmetry constraints (such as half- or quarter-domain simulations), ensuring that the flow symmetry emerges naturally from the governing equations.

Using a linear solver (discretising the LNSE around the present base flow solution), the large-scale eigenvalue problem (2.7) is then solved, as described in § 2.4.1. The results are reported in [figures 5\(a\)](#) and [5\(c\)](#). [Figure 5\(a\)](#) represents the eigenspectra in the σ – St^L (where the superscript L denotes results obtained from linear analysis) plane corresponding to three distinct Reynolds numbers and based on the orthogonal-symmetric steady base flow shown in [figure 4](#) (St^L and ω are linked by the relation $St^L = \omega/(2\pi)$). These eigenspectra indicate the destabilisation of the base flow as a purely real eigenvalue ($St^L = 0$) migrates into the positive σ half-plane, uncovering a pitchfork bifurcation.

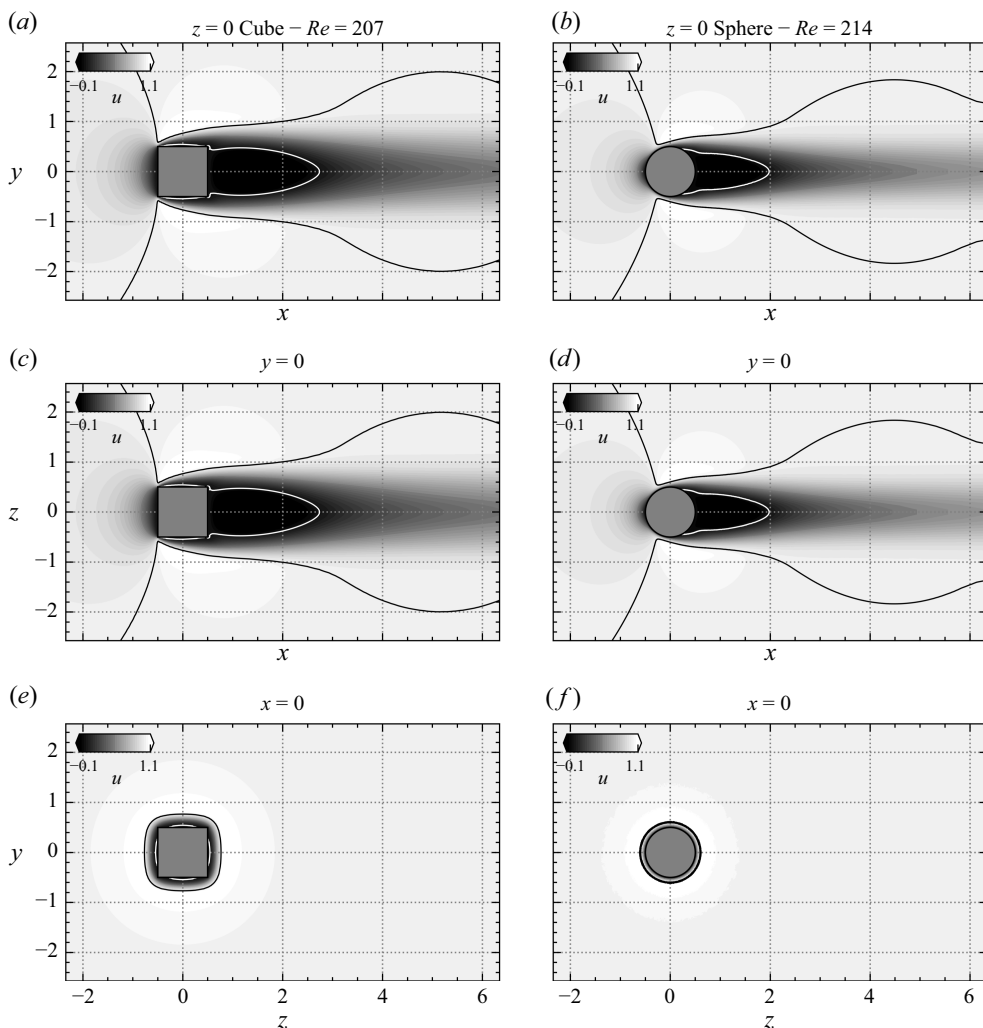


Figure 4. Comparative visualisation of base flows at the onset of a primary pitchfork bifurcation. (a,c,e) Orthogonallysymmetric steady base flow around a cube at a supercritical $Re = 207 > Re_{c,1}$. (b,d,f) Axisymmetric steady base flow around a sphere at a supercritical $Re = 214 > Re_{c,1}$. For each geometry, the figure is extracted at perpendicular cross-sections $z=0$, $y=0$ and $x=0$. Streamwise velocity maps with $u \in [-0.1, 1.1]$ are overlaid by white isolines for $u=0$, which delineate the recirculation regions indicative of reverse flow, and black isolines for $u=1$, highlighting the freestream flow.

Figure 5(c) illustrates the relationship between the amplification rate σ and the Reynolds number. We systematically sampled Reynolds numbers from $Re = 200$ to $Re = 212$ with increments $\Delta Re = \{3, 2, 1, 1, 2, 3\}$, ensuring a monotonically increasing sequence. This sampling strategy reveals a clear linear trend in the amplification rates as the Reynolds number increases. The monotonic nature of this relationship allows for reliable linear interpolation, enabling us to estimate the primary bifurcation threshold with high accuracy. Using this method, we determine that the critical Reynolds number is $Re_{c,1}^L = 206.39$. This value is closely aligned with those reported in the literature (cf. § 1.2.4 and tables 3, 4).

Sphere. Adopting a similar analytical trajectory for the sphere, over Reynolds numbers $Re = 207$ to $Re = 219$ with an identical ΔRe step sequence, we identified an axisymmetric yet unstable base flow at $Re = 214$, shown in figure 4(b,d,f). From this base flow, the

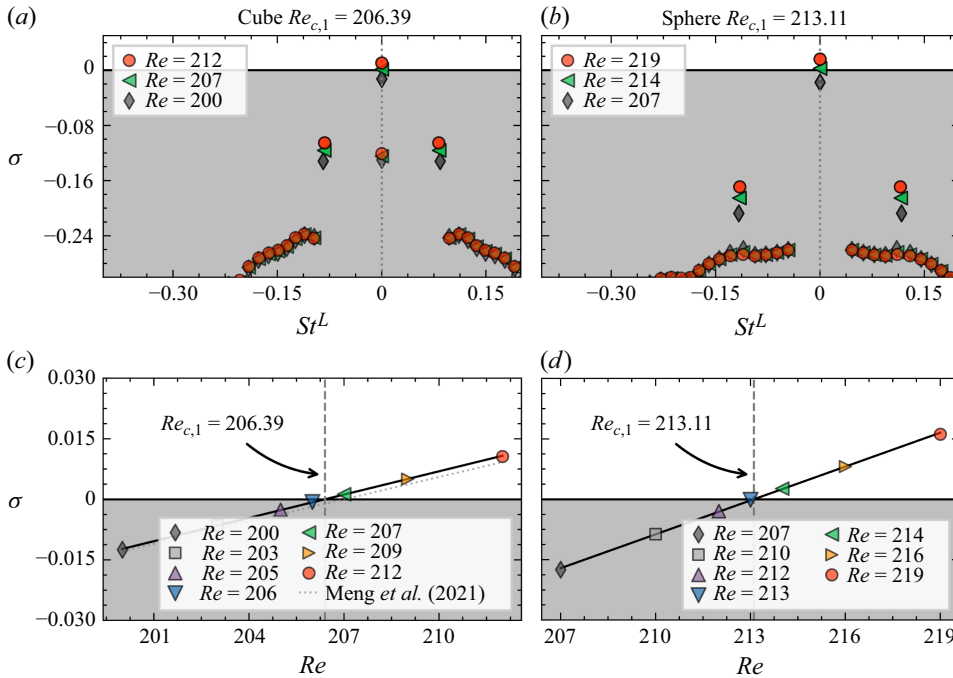


Figure 5. Primary bifurcation for (a,c) the cube and (b,d) the sphere. (a,b) Eigenspectra in the $\sigma - St^L$ plane, based on the steady symmetric base flow, evidencing a pitchfork bifurcation. (c,d) Trajectory of the leading eigenvalue's amplification rate σ in relation to the Reynolds number Re . The vertical dashed line defines the critical Reynolds number $Re_{c,1}^L = 206.39$ for the cube case, interpolated from the fitting linear equation $\sigma(Re) = 0.0019 \cdot (Re - Re_{c,1}^L)$ in panel (c) and $Re_{c,1}^L = 213.11$ for the sphere case, interpolated from the fitting linear equation $\sigma(Re) = 0.0028 \cdot (Re - Re_{c,1}^L)$ in panel (d).

eigenspectra analysis reported in figures 5(b) and 5(d) determines the primary (pitchfork) bifurcation threshold for the sphere at $Re_{c,1}^L = 213.11$. This threshold is in agreement with the literature-reported value of $Re_{c,1} \approx 212$ (cf. § 1.2.1 and tables 3, 4).

Discussion and comparison. By comparing cube and sphere base flows (figure 4), it can be observed that for an identical distance to $Re_{c,1}^L$, the recirculation length behind the cube is longer than that of the sphere. This may be explained by the presence of the secondary recirculation bubble formed along the lateral and top/bottom faces of the cube (see the $u = 0$ isolines in figure 4a,c,e), which participates in the elongation of the main recirculation zone behind the cube (Klotz *et al.* 2014). In their study, Meng *et al.* (2021) also evidenced the presence of four additional pairs of vortices generated on the lateral faces of the cube, directly ‘feeding’ the main vortex core. This phenomenon does not exist in the sphere case due to the curvature of the body, which prevents the formation of any secondary recirculation bubble.

Concerning eigenanalysis, we observed that at the respective critical values $Re_{c,1}^L$, the emergence of a positive real eigenvalue signals a pitchfork bifurcation for both geometries. This bifurcation marks the destabilisation of spatial symmetry, heralding a transition from a maximally symmetric wake to a planar symmetric state as the Reynolds number surpasses $Re_{c,1}^L$. Furthermore, figure 6 shows the unstable mode of the primary (pitchfork) instability, capturing its development in proximity to the steady symmetric fixed point (i.e. at $Re \approx Re_{c,1}$) for both cube and sphere configurations. The isosurfaces of the components of the perturbation velocity field show identical spatial symmetries in the (x, y) and

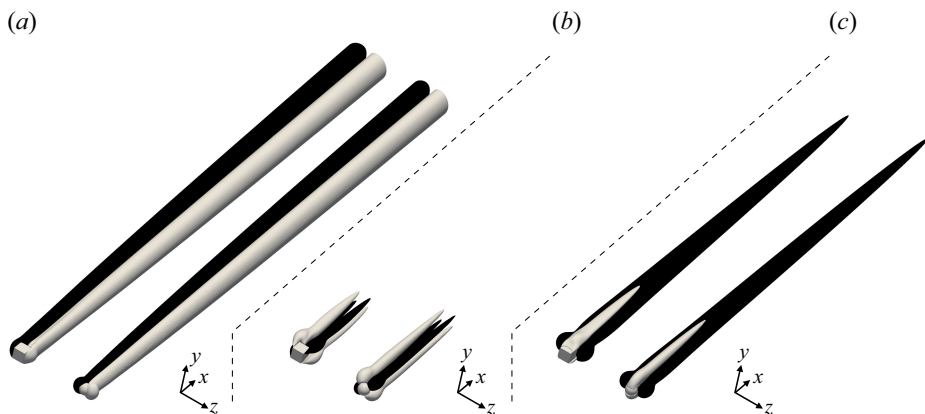


Figure 6. Primary bifurcation. Three-dimensional view of isocontours of (a) streamwise (u'), (b) vertical (v') and (c) spanwise (w') perturbation velocities plotted for the levels ± 0.01 of the real part of the leading unstable mode at $Re = 207$ for the cube case and $Re = 214$ for the sphere case.

(x, z) planes between the cube and the sphere case. These results therefore lead us to the conclusion that the corner-induced vortices which induce secondary flows around the cube surface do not impact the global dynamics, but act as an extra source making the main recirculation bubble larger and therefore destabilising the flow faster. This is captured by the lower critical Reynolds number in the cube case.

4. Secondary bifurcation

Our investigation of secondary bifurcations looks into the post-primary instability dynamics in both cube and sphere configurations.

Cube. At $Re = 245$, surpassing the primary instability threshold, a direct simulation in the cube scenario revealed a transition to a non-orthogonal asymmetric steady wake. We then performed a rigorous stability analysis, employing the Newton–Krylov solver to compute new fixed points, uncovering a planar-symmetric base flow which is temporally unstable at $Re = 252$, delineated in figure 7(a,c,e). The corresponding eigenspectra, depicted in figure 8(a), show a pair of complex conjugate eigenvalues (i.e. with $St^L \neq 0$) that become unstable as the Re increases from 245 to 257, exhibiting the emergence of an Hopf bifurcation and a fundamental frequency St_1^L , responsible for periodic vortex shedding in the wake region. Then, figure 8(c) gives the linear relation between σ and Re , for Reynolds numbers ranging from $Re = 245$ to $Re = 257$ with steps $\Delta Re = \{3, 2, 1, 1, 2, 3\}$, allowing us to estimate the secondary bifurcation threshold at $Re_{c,2}^L = 250.61$. This critical value aligns with the ranges reported in the literature, notably by Khan *et al.* (2020b) ($250 < Re_{c,2} < 276$) and Meng *et al.* (2021) ($Re_{c,2} \approx 252$). Using this interpolated critical value, we can interpolate again and obtain the associated critical frequency $St_{c,1}^L = 0.0927$, highlighted by the dash-dotted vertical line in figure 8(a). We note that the estimated critical frequency is also in very good agreement with the frequency $St_1 = 0.0975$ found by Meng *et al.* (2021) in their nonlinear simulations at $Re = 270$.

Sphere. Similarly, the Newton–Krylov solver computes an unstable planar-symmetric base flow for the sphere at $Re = 275$ (figure 7b,d,f) and the stability analysis, showcased in figures 8(b) and 8(d) and spanning from $Re = 268$ to $Re = 280$, led to the interpolation of the secondary bifurcation (Hopf) threshold at $Re_{c,2}^L = 273.67$ and to an estimated critical fundamental frequency equal to $St_{c,1}^L = 0.1282$. These findings are in close agreement

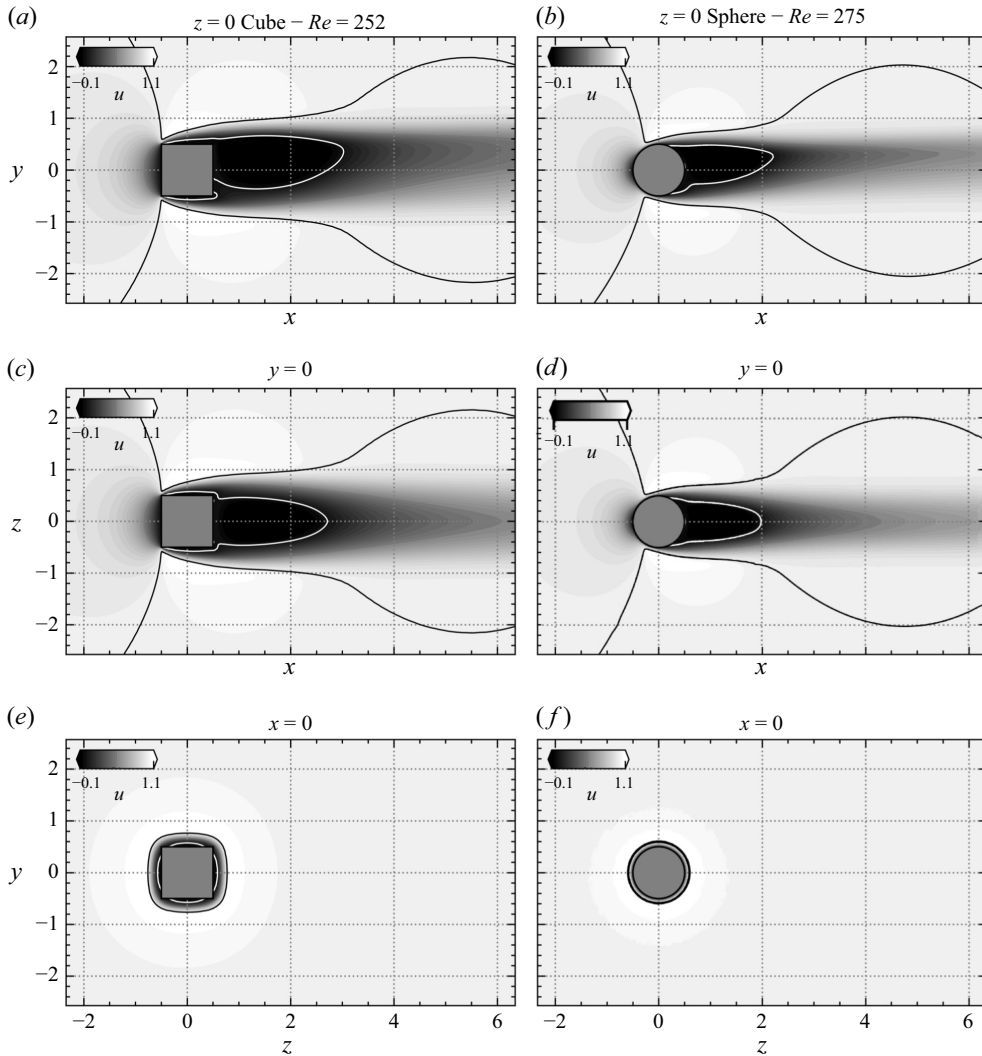


Figure 7. Comparative visualisation of base flows at the onset of a secondary Hopf bifurcation. (a,c,e) Planar-symmetric steady base flow around a cube at a supercritical $Re = 252 > Re_{c,2}$. (b,d,f) Planar-symmetric steady base flow around a sphere at a supercritical $Re = 275 > Re_{c,2}$. For each geometry, the figure is extracted at perpendicular cross-sections $z = 0$, $y = 0$ and $x = 0$. Streamwise velocity maps with $u \in [-0.1, 1.1]$ are overlaid by white isolines for $u = 0$ and black isolines for $u = 1$.

with the thresholds found in the literature ($Re_{c,2} = 275 \pm 6$) (cf. § 1.2.1 and tables 3, 4) and specifically with the stability analysis conducted by Citro *et al.* (2017) ($Re_{c,2} = 271.8$ and $St_{c,1} = 0.129$), emphasising the precision of the present methodology.

Discussion and comparison. This stability analysis first highlights striking similarities between the cube and sphere base flows, as well as in the unstable global eigenmode associated with the secondary bifurcation (Hopf), as shown in figure 9. In terms of discrepancies between the two bluff bodies, one can notice from the base flow computation (cf. figure 7), and for the same reason as that explained at the end of § 3, the recirculation length L_r for the cube is longer than the sphere's counterpart $L_r^{cube} > L_r^{sphere}$. The stability analysis then emphasises that the critical shedding frequency in the cube case is

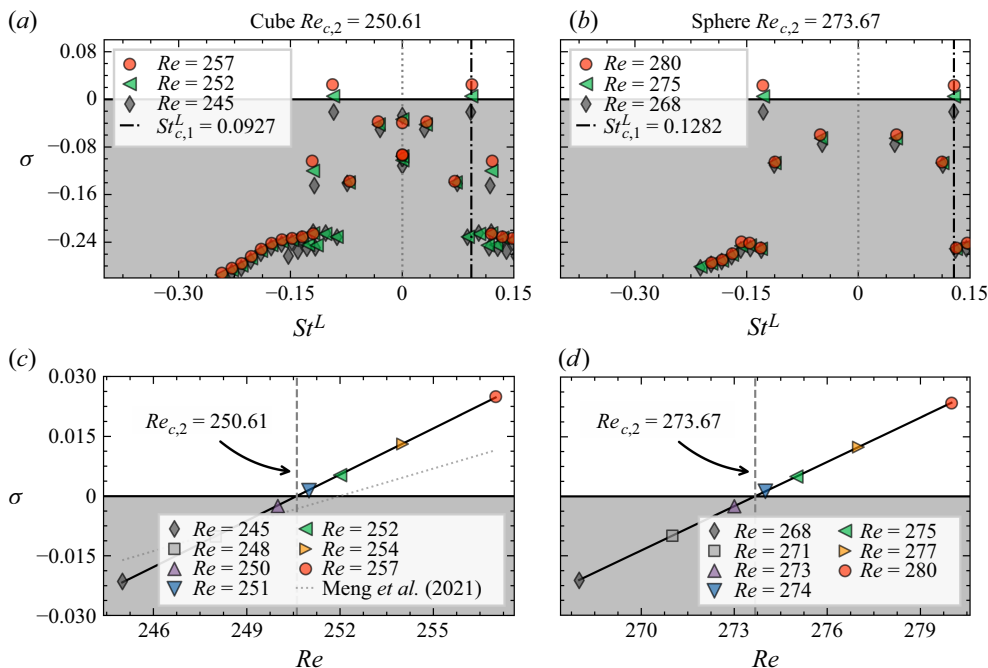


Figure 8. Secondary bifurcation for (a,c) the cube and (b,d) the sphere. (a,b) Eigenspectra in the $\sigma - St^L$ plane, based on the bifurcated steady planar-symmetric base flow, evidencing a Hopf bifurcation. (c,d) Evolution of the amplification rate with respect to the Reynolds number. The vertical dashed line defines the critical Reynolds number $Re_{c,2} = 250.61$ for the cube case, interpolated from the fitting linear equation $\sigma(Re) = 0.0039 \times (Re - Re_{c,2})$ in panel (c) and $Re_{c,2} = 273.67$ for the sphere case, interpolated from the fitting linear equation $\sigma(Re) = 0.0037 \times (Re - Re_{c,2})$ in panel (d).

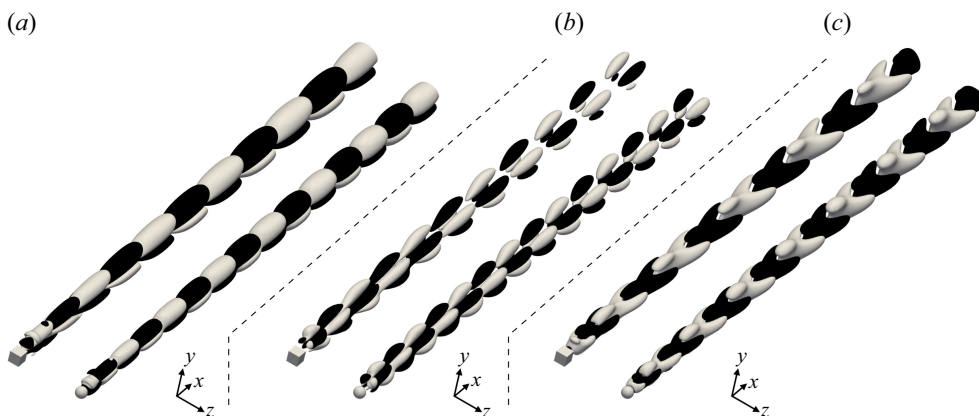


Figure 9. Secondary bifurcation. Three-dimensional view of isocontours of (a) streamwise (u'), (b) vertical (v') and (c) spanwise (w') perturbation velocities plotted for the levels ± 0.01 of the real part of the periodic leading unstable mode associated to the shedding frequency St_1 , at $Re = 252$ for the cube case and $Re = 275$ for the sphere case.

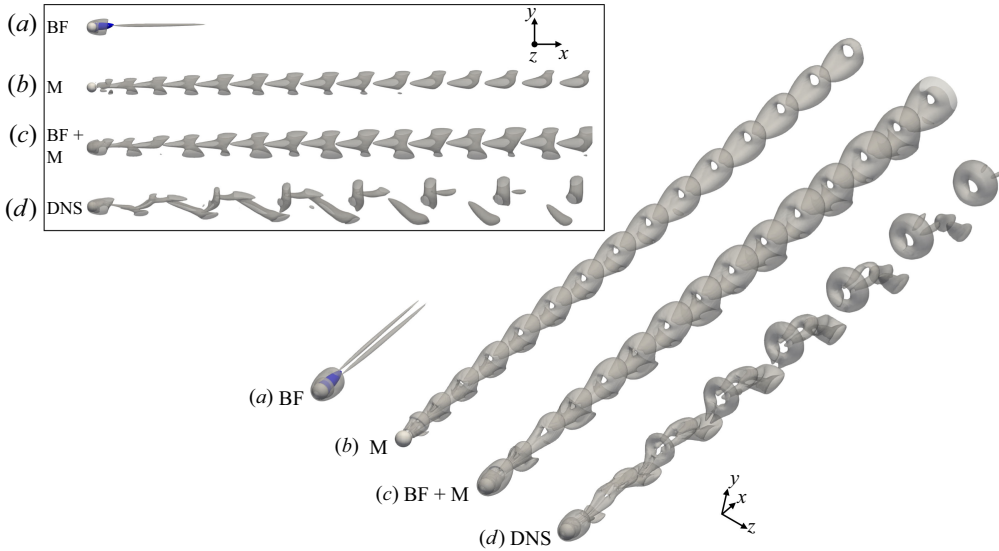


Figure 10. Secondary bifurcation at $Re = 275$ (sphere case only). Ω_r isocontours of: (a) ‘BF’, planar-symmetric steady base flow; (b) ‘M’, secondary unstable global eigenmode; (c) ‘BF + M’, linear combination of the base flow and global eigenmode at an arbitrarily fixed amplitude; (d) ‘DNS’, nonlinear solution. The top-left box shows a side view. [Movie 1] (cube), [Movie 2] (sphere).

lower than that of the sphere, $St^{cube} < St^{sphere}$ (figure 8) and that the opposite relation stands regarding the streamwise wave length Λ of the unstable mode, i.e. $\Lambda_{cube} > \Lambda_{sphere}$ (qualitatively observable in figure 9). The existence of a proportional dispersion relation between Λ and St in the range of Reynolds numbers under consideration in this study implies that $\Lambda_{cube} > \Lambda_{sphere} \Rightarrow St^{cube} < St^{sphere}$, and having the following relation between the recirculation length and wave length $L_r^{cube} > L_r^{sphere} \Rightarrow \Lambda_{cube} > \Lambda_{sphere}$ therefore makes the quantitative discrepancies between the cube and the sphere cases in terms of L_r , St and Λ values naturally correlated.

We now turn to examining the spatial mechanisms that drive the dynamical evolution of the planar-symmetric base flow following the Hopf bifurcation. Figure 10 presents a synchronised comparison of Ω_r -criterion isocontours for the sphere case, illustrating: (a) the planar-symmetric base flow (BF); (b) the unstable global eigenmode (M); (c) the linear superposition of base flow and eigenmode at a fixed amplitude (20 % of the maximum streamwise velocity of BF) that clearly reveals the eigenmode’s effect (BF + M), and (d) the direct numerical simulation at $Re = 275 > Re_{c,2}^L$ (DNS). The Ω_r -criterion employed in figure 10 follows the Omega-Liutex/Rortex methodology (Dong, Gao & Liu 2019), which identifies vortices by quantifying the ratio of local rigid-rotation vorticity component to total vorticity (rotation + deformation). A distinctive advantage of this criterion is its robust threshold value of $\Omega_r = 0.52$, which serves as a case-independent demarcation for vortex boundaries. When $\Omega_r > 0.52$, the rotational component dominates the deformation component, effectively capturing both weak and strong vortical structures within the same flow domain – an improvement over previous criteria that relied on *ad hoc*, flow-dependent thresholds.

We note that the fundamental mechanisms at play in the cube case are equivalent, so for clarity and conciseness, the following explanation focuses on the sphere’s spatial flow structures. The ‘DNS’ part of figure 10 clearly shows the well-known periodic vortex-shedding process, featuring alternating hairpin-like structures. In our view, this

phenomenon aligns with the minimal flow-elements model proposed by Cohen, Karp & Mehta (2014), which provides a ‘recipe’ for generating packets of hairpin vortices in shear flows. Their model – consisting of a shear flow, a counter-rotating vortex pair (CVP) and a streamwise oscillation – explains the mechanics of the instability leading to hairpin vortices and, more precisely, how the CVP modifies the base flow to create an inflection point, thereby amplifying the wavy vortex sheet. This amplification, in turn, destabilises the CVP, leading to its segmentation and the formation of hairpin vortex packets. Analysing more precisely the vortex shedding process in the present case, and as already observed in many numerical and experimental studies (Sakamoto & Haniu 1990; Johnson & Patel 1999; Kim & Choi 2002), the vortices shed from the sphere are alternating in a non-symmetric fashion in the (x, y) plane, with the creation of hairpin rings occurring in an apparently fixed orientation, namely, in the upper branch of the wake. The present figure 10 provides more detail on this phenomenon by spatially representing the eigenmode’s action on the base flow. In fact, in the part ‘(BF + M)’ of the figure, a delayed spatial amplification of the structures formed in the lower branch of the wake can be observed compared with their counterparts formed in the upper branch. This delay in amplification is directly related to the asymmetry of the base flow in the (x, y) plane, with a recirculation bubble shifted in the upper half (x, y) plane, implying different local velocity gradients in the two half-planes. Due to nonlinear effects, the amplification delay observed in the spatial structures of the eigenmode (M) and its linear superimposition with the base flow (BF + M) manifests in the ‘DNS’ solution with the formation of non-alternating hairpin rings (horseshoe-shaped). These rings are aligned with the orientation of the asymmetric base flow recirculation zone.

Base flow asymmetry and hairpin formation. In other words, the formation of hairpin vortices in the nonlinear flow can be traced back to the interplay between the asymmetric base flow and the unstable eigenmode. Although the linear mode alone does not manifest as a clear hairpin, it provides the initial ‘seed’ of vorticity perturbation. Because the base flow is vertically asymmetric (due to the pitchfork bifurcation), amplification differs between the upper and lower parts of the wake (i.e. local gradients), causing a noticeable lag or phase shift in vortex roll-up. By visualising the superposition of the base flow and the linear mode, one sees that the spatial evolution of the instability directly depends on local velocity gradients; the upper region of the wake experiences earlier, stronger amplification, while the lower region lags behind. In fully nonlinear simulations, this asymmetry in amplification eventually leads to hairpin structures forming predominantly on one side first, corroborating the linear predictions that spatial gradients in the base flow drive an uneven – yet ultimately coherent – shedding pattern.

5. Tertiary bifurcation

As previously shown, a limit cycle associated with periodic dynamics is created in the vicinity of the steady planar-symmetric fixed point when the secondary bifurcation (first Hopf) occurs. The investigation of tertiary bifurcation through linear stability analysis thus implies the computation and the stabilisation of the periodic base flow (a periodic orbit). In this section, we present results of the stability characterisation of stabilised periodic orbits based on Floquet theory. We present what we believe to be the first computation of three-dimensional Floquet modes, which reveal instabilities within the limit cycle and indicate the onset of tertiary bifurcations. To the best of our knowledge, the stability analysis of tertiary bifurcations in the flow past a cube and a sphere has not been previously reported. Therefore, in this section, we present the results not in terms of the ‘cube’ and ‘sphere’ cases sequentially, but by following the two main steps of the Floquet analysis:

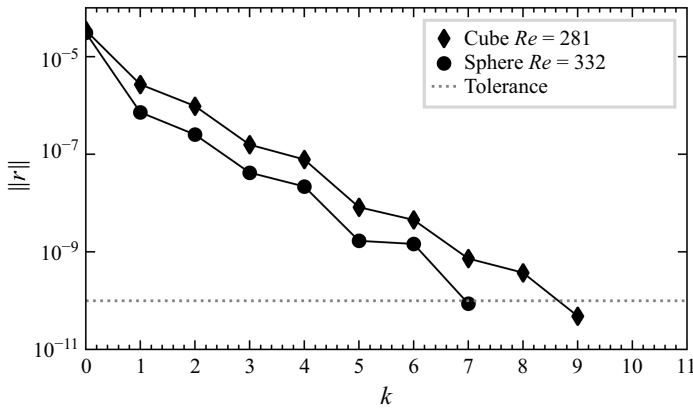


Figure 11. Residual deflation as a function of Newton–Krylov iterations (k) for the stabilisation of unstable periodic orbits (UPOs) in the cube and sphere cases. The initial solutions correspond to solutions at $Re = 280$ for the cube and $Re = 330$ for the sphere. Due to the proximity of these initial solutions to the target solutions, the initial residuals are of the order of 10^{-4} . The dotted line represents the specified tolerance level, while the curves demonstrate the convergence of the residual norm ($\|r\|$).

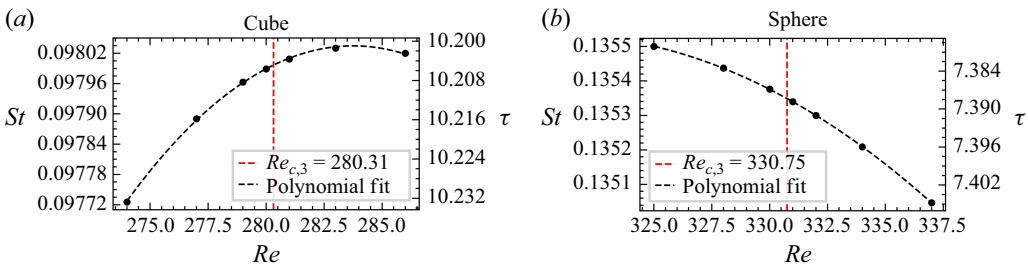


Figure 12. Strouhal numbers (St) and periods (τ) of the limit cycle computed using the Newton–GMRES solver as functions of the Reynolds number (Re) in (a) the cube case and (b) the sphere case. The black dashed lines represent second-order polynomial fits to the data points.

(i) computation of the periodic base flows for the cube and sphere; and (ii) computation of the Floquet modes for both obstacles.

Computation and analysis of the UPO. Figure 11 illustrates, for both cube and sphere cases, the residual reduction during the Newton–Krylov algorithm used for the computation of periodic orbits (cf. Appendix D.2). Figure 12 delineates the variation of the limit cycle frequency St and related period τ against the Re , using the Newton–Krylov solver to stabilise periodic orbits with naturally selected periods for both cases. We used initial guesses for the orbit period based on the frequency peak from the lift coefficient timeseries from preliminary simulations. The data highlight a discernible trend, fitted with a second-order polynomial, along with the critical Re interpolated from linear stability analysis results (presented hereafter). In particular, the critical frequency of the periodic base flow is interpolated and depicted for comparative analysis. Preliminary DNS at subcritical Re provided a robust initial estimate for the orbit period. This allowed a gradual increment of the Re to supercritical values, ensuring proximity to the desired solution branch and thus ensuring convergence of the Newton method.

A visualisation of the stabilised unstable limit cycle around the cube at supercritical Reynolds number $Re = 281 > Re_{c,3} = 280.31$ and around the sphere at supercritical Reynolds number $Re = 332 > Re_{c,3} = 330.75$, is shown in figure 13. The stabilised orbit

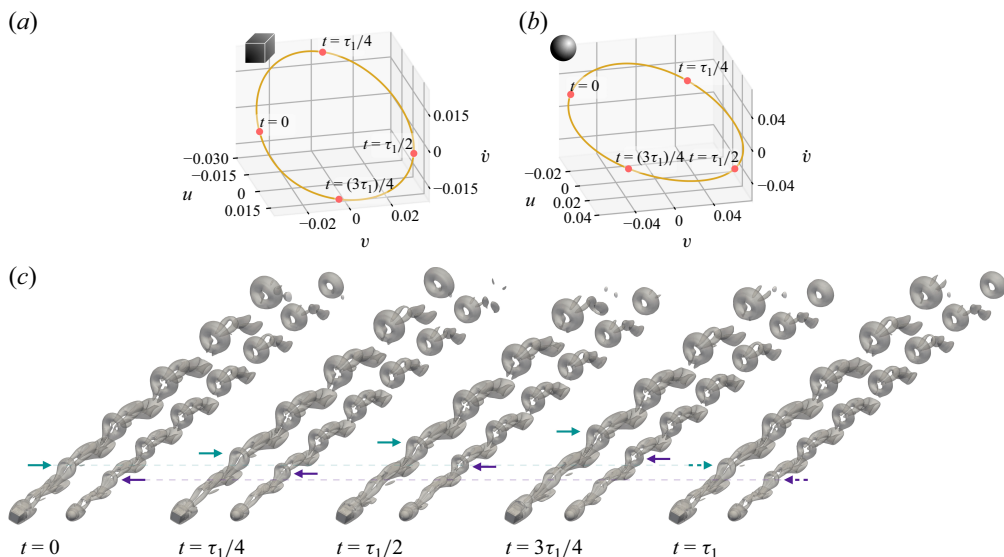


Figure 13. Comparative visualisation of the stabilised unstable limit cycle (i.e. periodic base flow) at the onset of a tertiary Neimark–Sacker bifurcation, at $Re = 281 > Re_{c,3}$ for the cube case and $Re = 332 > Re_{c,3}$ for the sphere case. (a and b) $(u, v, \partial v / \partial t)$ phase-portrait of periodic base flow in cube and sphere case, respectively. (c) Perspective view of $\Omega_r = 0.52$ isocontours of the periodic base flow represented for every quarter period of a shedding cycle. Green and purple arrows depict, in the cube and sphere case, respectively, the spatial location of a given hairpin through a complete shedding period τ_1 .

period τ is here denoted as τ_1 . The $\Omega_r = 0.52$ isocontours (figure 13c) are plotted at every quarter of the shedding period τ_1 , showing the periodic shedding of the hairpin vortical structures and their transport in the wake. Notably, there is a perfect match between the snapshots of the UPO at $t = 0$ and $t = \tau_1$. The time-periodic base flow of flow past the cube and the sphere are also represented by the $(u(t), v(t), \partial_t v(t))$ phase-portraits (figure 13a,b), depicting for both obstacles a clear limit cycle of period τ_1 . Figure 14 represents the stabilised UPO at $t = 0$ in different perpendicular cross-sections, highlighting the planar-symmetry of the periodic base flow for both the cube and the sphere.

Computation and analysis of the Floquet modes. Figure 15 represents the results of the Floquet stability analysis (cf. § 2.4.2) for the cube (panels a, c, e) and the sphere case (panels b,d,f). Figures 15(a) and 15(b) display for each obstacle the eigenspectrum of the Floquet multipliers μ_i (corresponding to the eigenvalues of the monodromy matrix \mathbf{M}_τ) relative to the unit disk $|\mu| = 1$, where the inner grey area represents the stable portion of the spectrum. For both cube and sphere, this eigenspectrum reveals the evolution of a complex conjugate pair of multipliers, progressively leaving the unit circle out of the $\mathcal{Re}(\mu)$ axis as Re grows, indicating a Neimark–Sacker bifurcation (also called a secondary Hopf bifurcation). As a result, the mode associated to a new frequency St_2 (incommensurate with respect to the shedding frequency St_1 that arises after the onset of the first Hopf bifurcation) becomes unstable, leading to quasiperiodic dynamics (the quasiperiodic regime will be temporally and spatially analysed in § 6). Figures 15(c) and 15(d) give the mapping of the spectrum of the monodromy matrix (figure 15a,b) towards the corresponding spectrum in the $\sigma - St^L$ plane of the Jacobian matrix, following the relation $\lambda_i = \ln(\mu_i) / \tau$. Eventually, figures 15(e) and 15(f) portray the linear progression of the growth rates σ with respect to Re .

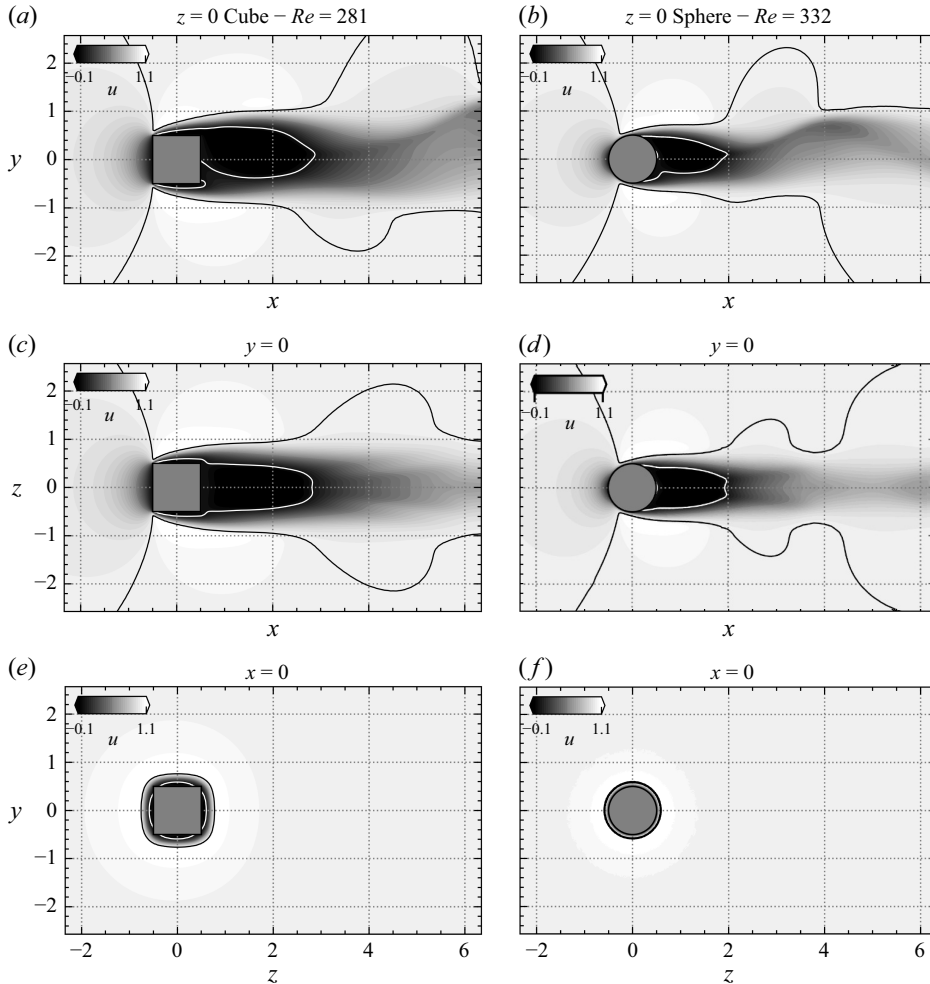


Figure 14. (Complement to figure 13). Comparative visualisation of a single snapshot on the stabilised unstable limit cycle in perpendicular cross-sections at $t = 0$, at the onset of a tertiary Neimark–Sacker bifurcation. The figure highlights the planar-symmetry of the cube and sphere’s stabilised periodic base flow.

Concerning the cube case, the tertiary bifurcation is identified at a critical Reynolds number of $Re_{c,3}^L = 280.31$ (figure 15e), aligning with DNS predictions of $Re_{c,3} = 282$ given by Meng *et al.* (2021). The new frequency of the unstable leading modes is interpolated from the critical value of $Re_{c,3}^L$ and is estimated to $St_{c,2}^L = 0.0276$ (see the vertical dash-dotted line in figure 15c), which matches the $St_2 = 0.0281$ value reported by Meng *et al.* (2021) in their nonlinear simulations at $Re = 282$.

Regarding the sphere case, the Neimark–Sacker bifurcation emerges at a critical Reynolds number of $Re_{c,3}^L = 330.75$ (figure 15f), which is slightly below the broad range of $350 < Re_{c,3} < 480$ reported in the DNS results of Kalro & Tezduyar (1998), Mittal (1999), Mittal & Najjar (1999), Lee (2000), Tomboulides & Orszag (2000). The new lower frequency is estimated to $St_{c,2}^L = 0.0385$ (see figure 15d), which lies in a reasonable range regarding the only available reference values reported at $Re = 500$ by Mittal & Najjar (1999) ($St_2 = 0.05$), Lee (2000) ($St_2 = 0.043$) and Tomboulides & Orszag (2000) ($St_2 = 0.045$). It is important to note that no hysteresis was observed. This was verified by

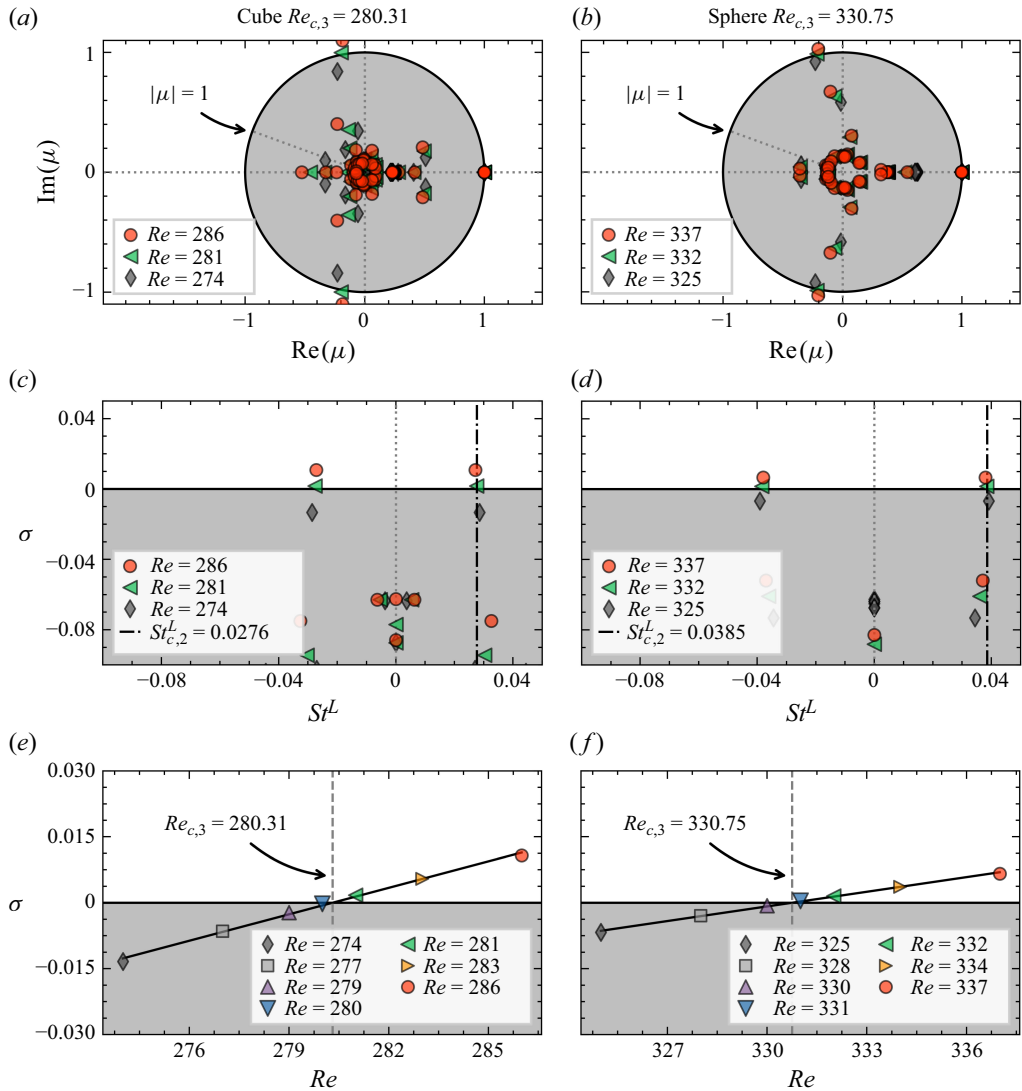


Figure 15. Tertiary bifurcation for (a,c,e) the cube and (b,d,f) the sphere. (a,b) Eigenspectra of the Floquet multipliers developing in the vicinity of the stabilised limit cycles at various Reynolds numbers, evidencing a Neimark–Sacker bifurcation. (c,d) Eigenspectra in the $\sigma - St^L$ plane, based on the stabilised limit cycles at various Re , evidencing the new frequency $St_{c,2}^L$. Note that zero eigenvalues corresponding to the base flow derivative are omitted from the plot. (e,f) Evolution of the amplification rate with respect to the Re . The vertical dashed line defines the critical Reynolds number $Re_{c,3} = 280.31$ for the cube case, interpolated from the fitting linear equation $\sigma(Re) = 0.0020 \cdot (Re - Re_{c,3})$ in panel (e) and $Re_{c,3} = 330.75$ for the sphere case, interpolated from the fitting linear equation $\sigma(Re) = 0.0011 \cdot (Re - Re_{c,3})$ in panel (f).

performing nonlinear simulations at a supercritical Re , followed by a gradual reduction of the control parameter. The system smoothly returned to the periodic state, confirming the supercritical nature of the third bifurcation for both the cube and sphere flows.

Finally, figure 16 presents the 3-D isocontours of the leading unstable eigenvector at $Re = 281 > Re_{c,3}$ for the cube and at $Re = 332 > Re_{c,3}$ for the sphere. This mode is associated to the new low-frequency St_2 and is therefore a periodic eigenfunction, of

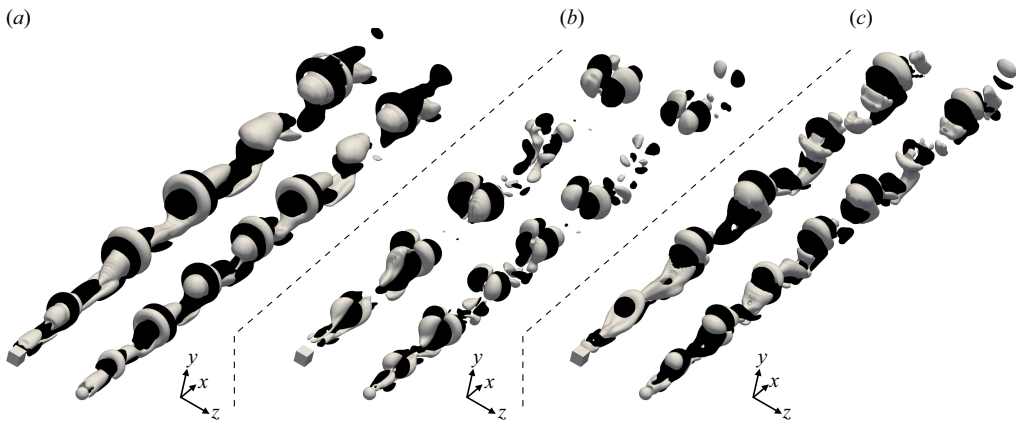


Figure 16. Tertiary bifurcation. Three-dimensional view of isocontours of (a) streamwise (u'), (b) vertical (v') and (c) spanwise (w') perturbation velocities plotted for the levels ± 0.01 of the real part of the periodic leading unstable mode associated to the secondary low-frequency St_2 , at $Re = 281$ for the cube case and $Re = 332$ for the sphere case.

Bifurcation	Cube		Sphere	
	Re_c^L	St_c^L	Re_c^L	St_c^L
I - Pitchfork	206.39	—	213.11	—
II - Hopf	250.61	0.0927	273.67	0.1282
III- Neimark–Sacker	280.31	0.0276	330.75	0.0385

Table 1. Summary of the present linear stability analysis with critical Reynolds numbers (Re_c^L) and critical Strouhal numbers (St_c^L). All bifurcations are of supercritical nature.

period τ_2 , represented in [figure 16](#) by a snapshot extracted at the beginning of this period. This eigenvector, emerging in the vicinity of the UPO, leads to the Neimark–Sacker bifurcation. It exhibits complex structures that are very comparable between the cube and the sphere case.

As an overview of the linear stability analyses performed in §§ 3, 4 and 5, [table 1](#) presents our linear predictions for the sequence of bifurcations, detailing the type, nature and critical thresholds in the flow past a cube and a sphere (a consistency verification of our critical frequencies for Hopf (II) and Neimark–Sacker (III) bifurcations is proposed in [Appendix C](#) by comparing them with frequencies extracted from nonlinear DNS at very similar values of Re). These results strongly support the conjectured sequence of: (I) pitchfork; (II) Hopf; and (III) Neimark–Sacker bifurcations in flows around CSC-BBs.

It should be noted that the critical values reported in this study are all based on the body diameter D as the characteristic length scale. Normalising Re_c^L and St_c^L using an alternative reference length scale could potentially collapse these critical thresholds for the cube and sphere cases, providing perhaps an even closer metric for flow behaviour across different body shapes, as suggested by attempts such as those of Gennaro, Colaciti & Medeiros (2013). However, upon closer inspection, it can easily be shown from [table 1](#) that this normalisation process cannot rely on the same length scale for Re_c^L and St_c^L values; and despite the fact that a length based on the size of the recirculation bubble appears to be a good candidate for such a normalisation procedure, our investigations found that it does not allow such unification across all bifurcations.

6. Dynamics of the quasiperiodic regime

This final section provides a detailed temporal and spatial characterisation of the flow dynamics in the quasiperiodic regime that emerges following the onset of the Neimark–Sacker bifurcation in both the cube and sphere cases. All analyses are based on DNS.

6.1. Temporal description

As previously mentioned, the quasiperiodic motion is characterised by two incommensurate fundamental frequencies St_1 and St_2 (i.e. $St_1/St_2 \notin \mathbb{Q}$), and the trajectory of the quasiperiodic system is represented by a curve on a so-called T^2 -torus that wraps around the torus without ever exactly repeating itself. To investigate in detail the dynamic nature of a quasiperiodic flow past a cube and a sphere, we use DNS. Our analysis focuses on the vertical lift coefficient, C_y , examining its time signal, power spectral density (PSD) and phase-space representation. This phase-space representation is augmented by the incorporation of the time derivative, $\partial_t C_y$, and the drag coefficient, C_x . The drag coefficient and the vertical lift coefficient are defined as follows: $C_x = F_x/(q\mathcal{A})$, $C_y = F_y/(q\mathcal{A})$, where $q = (1/2)\rho U_\infty^2$ with ρ being the fluid density, U_∞ and D the freestream velocity and the characteristic body length, and where F_x and F_y are the streamwise and vertical forces on the surface of the body, respectively, and \mathcal{A} the body reference area equal to $\mathcal{A} = D^2$ for the cube and to $\mathcal{A} = \pi D^2/4$ for the sphere. Since the spanwise component C_z is effectively zero within machine precision in the range of Re studied in this paper, we will therefore omit it from the visual representations.

It should be noted that our analysis relies on interpreting the temporal evolution of surface-integrated quantities, which, on the one hand, are relevant with respect to the global analysis performed in this work, and, on the other hand, correlate strongly with spatial probe data (e.g. velocity probes located in the wake) whose spectra show identical frequencies (see [Appendix E](#) for supporting results), thus indicating a robust synchronisation between the energy injected by the body and its redistribution by the wake for the considered Re .

[Figures 17\(a\)](#) and [17\(b\)](#) depict the C_y time signal, its PSD and the $(C_x, C_y, \partial_t C_y)$ phase-space representation of the flow past a cube and past a sphere at a Reynolds number slightly above the tertiary bifurcation point, that is, $Re = 282$ for the cube and $Re = 332$ for the sphere. Both signals span approximately 90 periods of the secondary frequency St_2 , ensuring fine precision in the identification of the PSD peak, and equivalent spectral resolution between the cube and sphere cases. From the right-hand sides of [figures 17\(a\)](#) and [17\(b\)](#), one can first observe that the curves drawn by the phase space representations clearly characterise a T^2 -torus. Concerning the Fourier spectra, one can identify two high-amplitude peaks corresponding to the fundamental frequencies St_1 and St_2 ($St_1 = 0.0975$ and $St_2 = 0.0281$ for the cube at $Re = 282$; $St_1 = 0.1338$ and $St_2 = 0.0392$ for the sphere at $Re = 332$), as well as their respective harmonics.

The other well-defined peaks in the PSD constitute a frequency comb centred around St_1 , with the constant offset St_2 and with peak intensities decreasing in the comb as $|k|$ increases (one refers to [figure 17c](#) for a sketch of a typical T^2 -torus Fourier spectrum). These frequencies arise from nonlinear triadic interactions between the two fundamental frequencies St_1 and St_2 , which satisfy the relation of the form $St_1 + kSt_2$ (with integer $k \in \mathbb{Z}$). This process is accompanied by a corresponding nonlinear energy transfer from the primary shedding mode to these newly formed frequencies.

This spectrum analysis aligns well with observations by Bohorquez *et al.* (2011), who provided, in the context of flow past blunt-based bluff bodies, a rare analysis of the secondary low-frequency arising in the quasiperiodic regime, stating that ‘the excitation

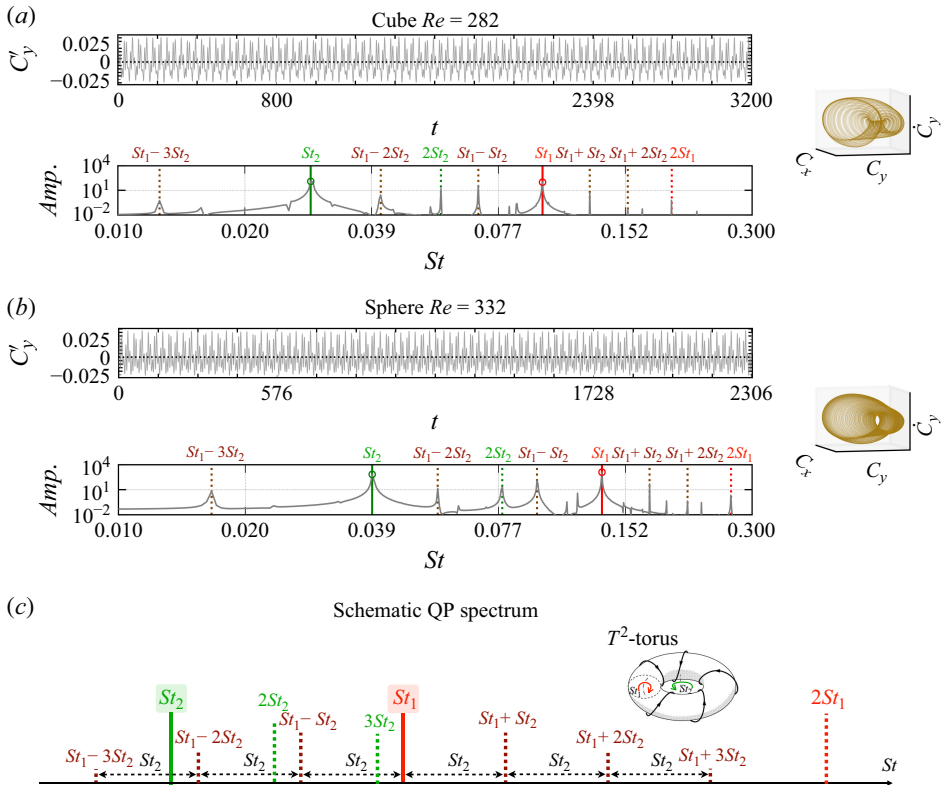


Figure 17. T^2 -torus in the quasiperiodic (QP) regime. The C_y time signal, its PSD and the $(C_x, C_y, \partial_t C_y)$ phase-space representation are shown for (a) the cube at $Re = 282$ and (b) the sphere at $Re = 332$. In each PSD, the primary frequency St_1 , the secondary frequency St_2 , their harmonics and the frequencies resulting from nonlinear triadic interactions are labelled. (c) Schematic of the frequency decomposition (in linear scale), showing how nonlinear triadic interactions generate frequency peaks of the form $St_1 + kSt_2$ ($k \in \mathbb{Z}$), separated by the constant offset St_2 . The fundamental frequencies St_1 and St_2 are incommensurate (i.e. $St_1/St_2 \notin \mathbb{Q}$).

of new frequencies in the wake (i.e. the low-frequency modulation and the harmonics of the main frequency) leads to a decrease of the energy associated with the leading velocity fluctuations due to the nonlinear energy transfer from the natural frequency (St_1) to the newly excited ones.' This redistribution of energy suggests that the Neimark–Sacker bifurcation plays a crucial role in initiating the transition towards a more complex, eventually turbulent, state by broadening the range of excited frequencies and slowly breaking the energy balance in the wake.

6.2. Spatial description

An intuitive way to grasp the tertiary bifurcation and the ensuing quasiperiodic regime is by examining the spatial flow structures associated with the unstable Floquet mode and contrasting them with the fully nonlinear flow fields obtained from DNS. This subsection discusses how the newly emerging low-frequency motion (St_2) combines with the primary shedding frequency (St_1) to produce modulated vortex dynamics in the wake.

Floquet mode structure. Figure 18 illustrates, for both cube and sphere cases, the three-dimensional Floquet mode (coloured in blue and red), that becomes unstable at the tertiary bifurcation, for every quarter of its own period τ_2 . The periodic base flow superimposed here in grey – already shedding at frequency St_1 – serves as the

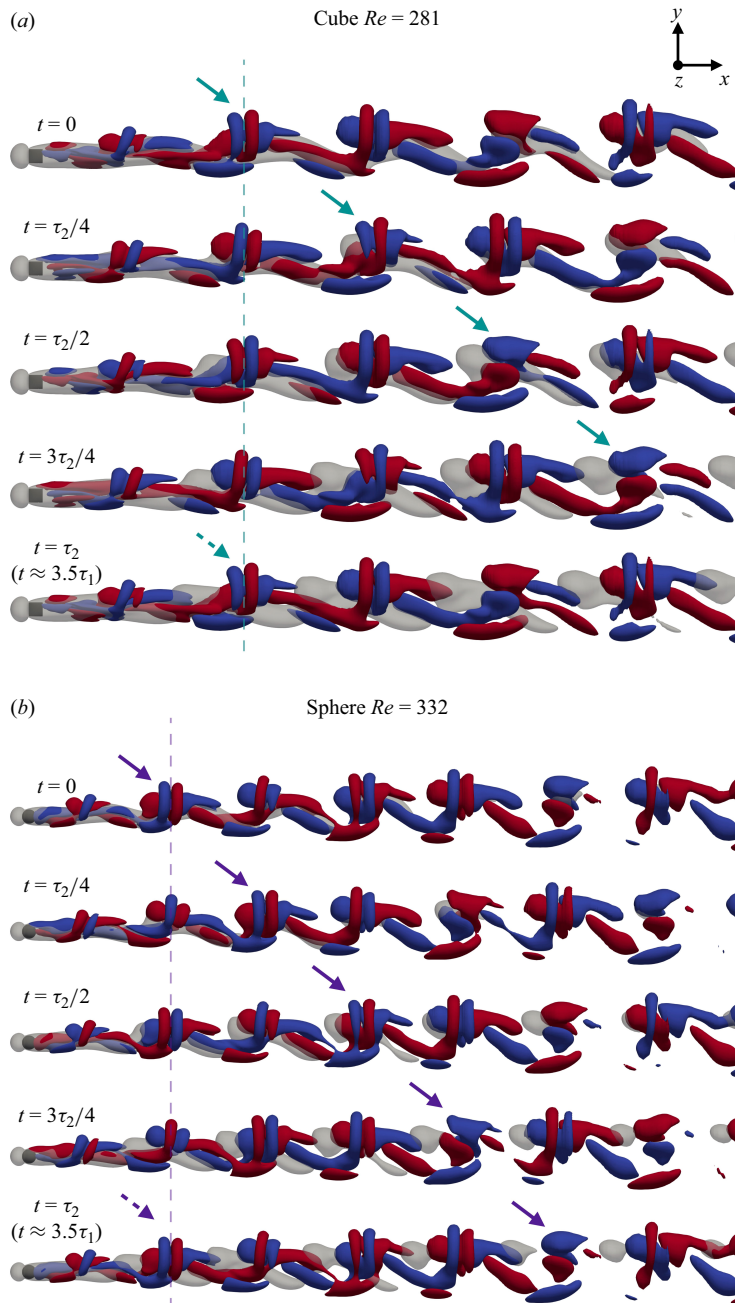


Figure 18. Superimposition of the streamwise velocity component of the periodic base flow, shedding at frequency S_{t1} (grey) with the real part of the leading unstable Floquet mode (streamwise component of velocity perturbation coloured with the levels -0.01 (blue) and 0.01 (red)) represented for every quarter period of the Floquet mode's period τ_2 . One notes that while the Floquet mode covered one period τ_2 , the periodic base flow covered $S_{t1}/S_{t2} \simeq 3.5$ shedding cycles of period τ_1 . (a) Cube case at $Re = 281$ [Movie 3]. (b) Sphere case at $Re = 332$ [Movie 4].

‘time-periodic equilibrium’. Spatially, one sees from the 3-D mode representation that velocity perturbations appear downstream of the body and extend through the wake, concentrating mostly around the hairpin heads. Moreover, the videos given as Supplementary material in figure 18’s caption allow one to notice that, for both obstacles, the Floquet mode does not propagate at constant speed along the base flow; it accelerates between two hairpins. The unstable mode therefore manifests as a gentle modulation or ‘waviness’ applied to the hairpin-like structures characteristic of the primary shedding. Since the velocity perturbations preserve the planar symmetry of the base flow, the Floquet mode does not disrupt the underlying reflectional symmetry. Instead, it introduces a slow, global oscillation in phase, which, as supported hereafter by the nonlinear results, manifests itself as a streamwise lag modulation between the heads of successive hairpin vortices.

Quasiperiodic dynamics. Figure 19 confirms the picture in figure 18 given by Floquet theory through DNS snapshots of the wake in the supercritical regime, where both frequencies St_1 and St_2 are excited. Unlike the single-frequency shedding observed in the previous periodic regime (cf. figure 13), the flow now develops an additional low-frequency modulation under the action of St_2 .

Exactly as observed by Meng *et al.* (2021) in the cube case, figures 19(c) and 19(d) clearly show that over approximately 7 periods of vortex shedding (i.e. $7\tau_1$), the cube’s and sphere’s wakes undergo approximately 2 cycles (i.e. $2\tau_2$) of shedding modulation. This observation is perfectly corroborated by figures 19(a) and 19(b) depicting for cube and sphere the time series of vertical velocity v along one quasiperiod. Additionally, the time series reveal that the vortex shedding is modulated both in phase and amplitude. This phase and amplitude modulation can be seen as a slow spatial drift which is due to the superposition of two incommensurate frequencies (St_1 from the original limit cycle, plus St_2 from the Floquet mode). This interplay produces a quasiperiodic wake, whose trajectory in phase space (e.g. lift C_y versus drag C_x) wraps around a two-dimensional torus rather than closing into a single cycle (see the phase portraits in figure 17). The fact that the quasiperiodic pattern is completed within approximately 7 periods of vortex shedding or 2 cycles of wake oscillation is directly linked to the $St_1/St_2 \approx 7/2$ ratio. In the present simulations, performed at supercritical Re close to the Neimark–Sacker bifurcation, the phase oscillation of the hairpin shedding manifests solely in the (x, y) plane (the flow remains planar-symmetric). However, one may hypothesise that as the Re increases to values not explored in this work, the flow could potentially develop additional three-dimensional shifts, perhaps showing a spanwise wobble in z , like that observed by Sakamoto & Haniu (1990) and Chrust *et al.* (2013).

7. Conclusions

This study investigated the bifurcation sequence governing the transition from steady to quasiperiodic dynamics in the wakes of compact-simplyconnected bluff bodies (CSC-BBs), focusing on the canonical cube and sphere cases as representative examples. Combining three-dimensional global linear stability analysis (LSA) and nonlinear simulations within a unified framework, this work confirms a consistent sequence of three supercritical bifurcations for these bodies: (I) a symmetry-breaking pitchfork; (II) a Hopf leading to periodic shedding (St_1); and (III) a Neimark–Sacker (St_2) leading to quasiperiodicity ($St_1/St_2 \notin \mathbb{Q}$). This analysis, performed within a cohesive numerical set-up, helps reconcile fragmented findings from the diverse literature by providing a systematic comparison and physical description.

Our findings clearly demonstrate that both cube and sphere flows, after losing initial spatial symmetries, traverse a single-frequency periodic regime before evolving into

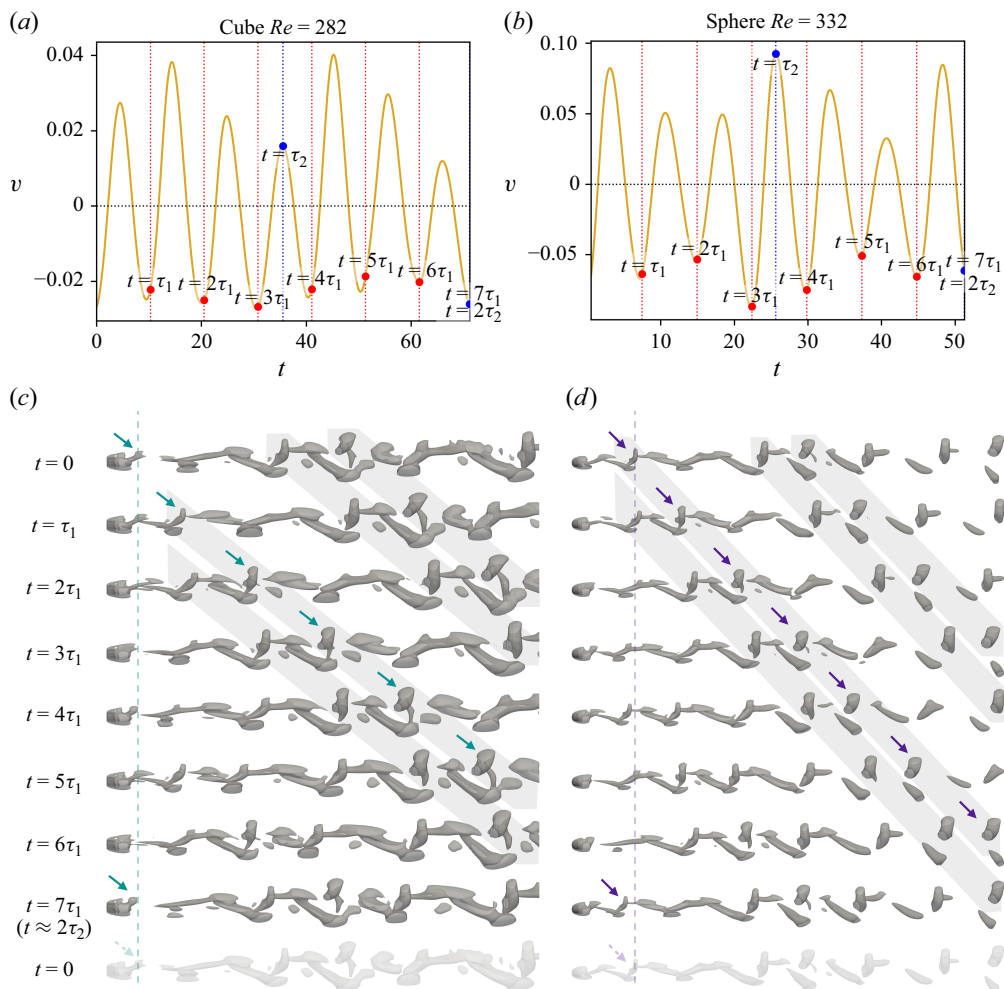


Figure 19. Quasiperiodic wake states for (a,c) cube at $Re = 282$ and (b,d) sphere at $Re = 332$, illustrating the interaction of two incommensurate frequencies. Panels (a) and (b) show timeseries of vertical velocity v , where the red markers indicate multiples of the primary period τ_1 , and blue markers the secondary period τ_2 . Panels (c) and (d) display isosurfaces of $\Omega_r = 0.52$ at selected multiples of τ_1 . The secondary frequency induces a convective modulation of the hairpin structures shedding (materialised by the non-equispaced grey bands), producing a quasiperiodic flow pattern that never repeats exactly. [Movie 5] (cube), [Movie 6] (sphere).

a quasiperiodic state characterised by two incommensurate frequencies, St_1 and St_2 , signifying a Neimark–Sacker bifurcation. A crucial contribution is the first direct identification of this bifurcation in fully three-dimensional bluff-body flows, achieved through a Floquet stability analysis on stabilised unstable periodic orbits, where the spatial structures of the unstable mode have been visualised and interpreted.

Furthermore, we characterise the quasiperiodic regime of cube and sphere wakes, in time and space. Nonlinear simulations clearly show spectra dominated by the two incommensurate frequencies (St_1, St_2) and combination tones arising from nonlinear interactions. Spatially, the analysis demonstrated how the unstable Floquet mode (associated with low-frequency St_2) modulates the primary hairpin vortex shedding pattern (driven by St_1) through phase and amplitude variations, preserving the flow's planar symmetry.

LSA and DNS revealed striking similarities for both cube and sphere flows, highlighting common underlying mechanisms despite body geometry differences. The similar bifurcation sequence for a flow past a cube (discrete symmetry) and a sphere (continuous symmetry) strongly supports its relevance as a route towards quasiperiodic dynamics for the broader CSC-BB class. These findings enhance the fundamental understanding of how self-sustained unsteadiness originates and evolves in bluff-body wakes.

A further open question is whether a truly universal scaling exists for the critical thresholds of all three bifurcations. Our preliminary investigations suggest that finding such a universal scaling may be non-trivial. Future work could also explore sensitivity analysis to external noise, ultimately guiding the design of more effective flow control strategies.

Another interesting avenue for future work would be to investigate the role of the CSC-BB's intrinsic symmetry in the flow dynamics when the Re increases after the onset of quasiperiodicity. Is the route to chaos identical for the flow around a cube and around a sphere? Elements in the literature seem to reveal that it is not the case. Meng *et al.* (2021) found for the cube a scenario of a period-doubling cascade before chaos, whereas for the sphere, Frantz (2022) and Sierra-Ausín *et al.* (2022) suggest a Ruelle–Takens–Newhouse scenario with the appearance of a third incommensurate frequency.

Ultimately, this research highlights how computer power, combined with Floquet theory, Krylov methods and dynamical systems concepts, can unlock insights into fluid dynamics, transforming our perception of complex transitional flows, revealing the simple yet elegant mechanisms that govern their behaviour.

Supplementary movies. Supplementary movies are available at <https://doi.org/10.1017/jfm.2025.10469>.

Acknowledgements. The authors are thankful to M. A. F. Meideros, S. Kern, A. Sansica, B. Semin and J. E. Wesfreid for fruitful discussions.

Funding. This work was funded by the French Ministry of Higher Education, Research, and Innovation (MESRI). This work was granted access to the HPC resources of IDRIS under the allocation Grant 2021-[A0112A06363], Grant 2022-[A0132A06363], Grant 2023-[A0152A06363] made by GENCI.

Declaration of interests. The authors report no conflict of interest.

Appendix A. Overview of literature and symmetry classifications

Temporal dynamics	
SS	Steady state
TP	Time periodic (single frequency vortex shedding)
QP	Quasi-periodic (double-incommensurable frequencies vortex shedding)
Spatial symmetries	
AS	Axisymmetry
OS	Orthogonal symmetry: symmetry in both vertical and spanwise planes
RS	Reflectional symmetry: planar symmetry
RSP	Reflectional symmetry preserving: preserves planar symmetry
RSB	Reflectional symmetry breaking: no planar symmetry
RSR	Reflectional symmetry recovering: recovers planar symmetry

Table 2. Summary of temporal dynamics and spatial symmetry used in this study.



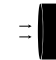
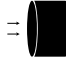
Bluff bodies	Regime I	Bifurcation I	Regime II	Bifurcation II	Regime III	Bifurcation III	Regime IV	Bifurcation IV	Regime V
AXISYMMETRIC									
 Sphere	SS - AS	Pitchfork $Re_c = 210 \pm 2$ [1,2] [3,4,5,6,7,8,9] [10,11,12,13]	SS - RS	Hopf $Re_c = 275 \pm 10$ [1,14,15,2] [4,5,6,7,8,9] [3,10,11,12,13]	TP - RSP	$350 \leq Re_c \leq 375$ [7,16] [17] $Re_c \leq 400$ [18] $Re_c \approx 420$ [14] $Re_c > 480$ [19]	Unsteady with two frequencies - ?	$Re_c > 480$ [14] $Re_c < 430$ [17]	Unsteady - RSB with periodic rotation of shedding plane
 Flat disk ($AR \ll 1$)	SS - AS	Pitchfork $Re_c = 115$ [20] $Re_c = 116.5$ [3] $Re_c = 117.1$ [21,11] $Re_c = 116.5(1 + AR)$ [22] $Re_c = 115(1 + AR)$ [23]	SS - RS	Hopf $Re_c = 121$ [20] $Re_c = 125.6$ [3] $Re_c = 123.7$ [21,11] $Re_c = 125.6(1 + AR)$ [22]	TP - RSB	$Re_c = 140$ [20] $Re_c = 143.7$ [21]	TP - RSR	$Re_c = 280$ (for $AR = 1/10$) [24]	Unsteady with two frequencies - RSB
 Thick disk ($AR = 1/3$) [25]	SS - AS	$Re_c = 159.4$	SS - RS	Hopf $Re_c = 179.8$	TP - RSP	$Re_c = 184 - 185$	Unsteady with two frequencies - RSB		
 Thick disk ($AR = 1$) [26]	SS - AS	Pitchfork $Re_c = 276$	SS - RS	Hopf $Re_c = 355$	TP - RSP	$Re_c = 395$	Unsteady with two frequencies - RSP		
 Falling Cone	SS - AS	Pitchfork $Re_c \approx 100$ [27]	SS - RS	Hopf $Re_c = 160$ (20°) [28] $Re_c = 155$ (40°) [28] $Re_c = 170$ (60°) [27]	TP - RSP	$Re_c = 300$ (60°) [27]	? - RSB		

Table 3. For caption see next page.


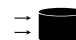
Bluff bodies		Regime I	Bifurcation I	Regime II	Bifurcation II	Regime III	Bifurcation III	Regime IV	Bifurcation IV	Regime V
	Blunt-based bluff body ($AR = 1$) [29]	SS - AS	Pitchfork $Re_c = 215$ (for DNS and glob. lin. stab.)	SS - RS	Hopf $Re_c = 254$ (DNS) and $Re_c = 267.6$ (expe)					
	Blunt-based bluff body ($AR = 2$) [29]	SS - AS	Pitchfork $Re_c = 319$ (DNS) and $Re_c = 327$ (glob. lin. stab.)	SS - RS	Hopf $Re_c = 413$ (DNS and expe)	TP - RSP	$450 < Re_c < 500$	Unsteady with two frequencies - RSP		
	Blunt-based bluff body ($AR \approx 6$)	SS - AS	Pitchfork $Re_c = 424$ [30]	SS - RS	Hopf $Re_c = 605$ [30] $Re_c = 577$ [29]	TP - RSP	$650 < Re_c < 675$ [30]	QP - RSP		
	Small cylinder ($AR = 1$) [31]	SS - AS	Pitchfork $Re_c = 172.2$	SS - RS	Hopf $Re_c = 282$	TP - RSP	$Re_c \approx 332$	Unsteady with two frequencies - ?		
	Small cylinder ($AR = 1.75$) [31]	SS - AS	Hopf $Re_c \approx 218$	TP - RSP	$Re_c \approx 240$	Unsteady with two frequencies - ?				
	Infinite cylinder ($AR = \infty$)	SS - AS (2D wake)	Hopf $Re_c = 46 \pm 1$ [32] [33,34,35]	TP - RSP (2D wake)	Secondary Pitchfork (subcritical - mode A) $Re_{cA} \approx 188$ [36,37] $Re_{cA} \approx 200$ [38]	TP - RSB (3D wake)	(supercritical - mode B) $Re_{cB} \approx 256$ [37] $Re_{cB} \approx 259$ [34]	Loss of spatio-temporal symmetry		

Table 3. For caption see next page.

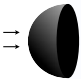
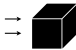
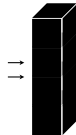

Bluff bodies	Regime I	Bifurcation I	Regime II	Bifurcation II	Regime III	Bifurcation III	Regime IV	Bifurcation IV	Regime V
WITH REFLECTIONAL SYMMETRY									
 Hemisphere [39]	SS - OS	$Re_c \approx 180$	SS - RS	$Re_c \approx 200$	TP - RSB	$Re_c \approx 220$	TP - RSR	$Re_c \approx 280$	Unsteady aperiodic - RSB
 Cube	SS - OS	$216 < Re_c < 218$ [40] $200 < Re_c < 215$ [41] $Re_c = 207$ [42] $Re_c = 186$ [43]	SS - RS	Hopf $265 < Re_c < 270$ [40] $Re_c = 285$ [43] $250 < Re_c < 276$ [41] $Re_c \approx 252$ [42]	TP - RSP	$300 < Re_c < 339$ [41] $Re_c \approx 281$ [42]	QP - RSP [42]		
 Square cylinder ($AR = \infty$)	SS - OS (2D wake)	Hopf $Re_c = 51.2$ [44] $Re_c = 53$ [45]	TP - RSP - ? (2D wake)	Secondary Pitchfork (mode A) $150 < Re_{cA} < 175$ [46]	TP - RSP (3D wake)	(mode B) $175 < Re_{cB} < 205$ [46]	TP - RSP		
 Ahmed body (with ground)[47]	SS - RS	Pitchfork $Re_c = 340$	SS - Asymmetric	Hopf $Re_c \approx 410$	Unsteady - Asymmetric				

Table 3. (cntd). Bifurcations and regimes for flows past 3-D bluff bodies (see table 2 for the meaning of temporal and spatial dynamics in ‘Regime’ columns). Full bibliographic references are provided at the end of the table. Colour code for the references: (blue) for experimental studies; (green) for DNS; (orange) for stability analysis + DNS; (purple) for stability analysis + DNS + experimental.

[1] Magarvey & Bishop (1961) [2] Szaltys *et al.* (2012) [3] Natarajan & Acrivos (1993) [4] Tomboulides, Orszag & Karniadakis (1993) [5] Johnson & Patel (1999) [6] Ghidersa & Dušek (2000) [7] Mittal (1999) [8] Thompson *et al.* (2001) [9] Constantinescu & Squires (2004) [10] Pier (2008) [11] Meliga *et al.* (2009b) [12] Citro *et al.* (2017) [13] Sansica *et al.* (2018) [14] Sakamoto & Haniu (1990) [15] Gumowski *et al.* (2008) [16] Mittal & Najjar (1999) [17] Chrust *et al.* (2013) [18] Kalro & Tezduyar (1998) [19] Lee (2000) [20] Fabre *et al.* (2008) [21] Meliga *et al.* (2009a) [22] Fernandes *et al.* (2007) [23] Bobinski, Goujon-Durand & Wesfreid (2014) [24] Shenoy & Kleinstreuer (2008) [25] Auguste *et al.* (2010) [26] Pierson *et al.* (2019) [27] Yaginuma & Itō (2008) [28] Goldburg & Florsheim (1966) [29] Bohorquez *et al.* (2011) [30] Rigas *et al.* (2017) [31] Yang *et al.* (2022) [32] Provansal, Mathis & Boyer (1987) [33] Jackson (1987) [34] Barkley & Henderson (1996) [35] Kumar & Mittal (2006) [36] Henderson & Barkley (1996) [37] Blackburn & Lopez (2003) [38] Karniadakis & Triantafyllou (1992) [39] Kim & Choi (2003) [40] Saha (2004) [41] Khan *et al.* (2020a) [42] Meng *et al.* (2021) [43] Klotz *et al.* (2014) [44] Sohankar *et al.* (1998) [45] Kelkar & Patankar (1992) [46] Robichaux *et al.* (1999) [47] Grandemange *et al.* (2012) [48] Marquet & Larsson (2015).

Appendix B. Mesh design and sensitivity

B.1. Domain size

The computational domain considered throughout the present work is defined by (In, Out, Sides) = $(10D, 50D, 10D)$, indicating the domain extends $10D$ upstream, $50D$ downstream and $\pm 10D$ laterally. To assess possible blockage effects, we calculate the blockage ratio, defined as the ratio of the cross-sectional area of the body to the cross-sectional area of the domain. For the cube, the blockage ratio is $D^2/(20D)^2 = 0.25\%$. For the sphere, it is $\pi(D/2)^2/(20D)^2 = \pi D^2/4/400D^2 \approx 0.20\%$. Both values are well below the threshold of 0.43% suggested by Klotz *et al.* (2014) to ensure negligible blockage effects.

In a relative point of view, for the cube case, our domain dimensions are larger in all directions compared with previous numerical studies. In fact, Meng *et al.* (2021) used domain dimensions of $7.5D$ upstream, $30D$ downstream and $\pm 7.5D$ laterally, while Saha (2004) used $6D$ upstream, $22D$ downstream and $\pm 7D$ laterally. For a clear quantitative comparison of the effects of domain size, the top part of table 4 summarises the domain sizes of previous studies in the literature associated with the critical Reynolds values $Re_{c,1}$ and $Re_{c,2}$, and the fundamental shedding frequency St_1 computed or measured in such domains.

For the sphere, our domain is comparable to or slightly larger than most prior studies (e.g. Citro *et al.* (2017) used $(10D, 30D, \pm 10D)$ in one configuration and $(14D, 38D, \pm 14D)$ in another). Only Meliga *et al.* (2009b) adopted a very extensive domain of $(100D, 200D, 25D)$ in the context of axisymmetric simulations. The bottom section of table 4 summarises these references. Overall, our chosen domain provides adequate space for flow development and exhibits sufficiently low blockage to mitigate boundary influences.

B.2. Mesh design and sensitivity

To simulate the wake dynamics around the cube and sphere, we designed two distinct multiblock grids specifically to each geometry. Both grids use smooth refinements and are composed of second-order hexahedral elements of low aspect ratio, thereby reducing numerical distortion and promote better convergence of iterative solvers (Fischer 1997).

For cube simulations, the mesh contains 49 176 elements, maintaining symmetry in y and z . The flat surfaces and sharp edges of the cube allow for a straightforward meshing strategy, focusing on resolving the regions near the wall and in the wake with high gradients. A 3-D mesh is constructed by, first, extruding a 2-D cross-section in the z -direction around the cube faces normal to z , and then filling the remaining corner regions. In contrast, sphere simulations required a more intricate mesh with 63 281 elements to capture curvature accurately. A butterfly meshing strategy was used, with a central element at the pole and surrounding elements that conform to the surface of the sphere.

The final meshes enabled our simulations to closely match the fundamental frequencies of the limit cycles reported in both experimental and numerical studies, as reviewed in the introduction. Table 5 compares our results with the finite-volume DNS of Meng *et al.* (2021) for the cube and the spectral-element stability analyses of Bouchet *et al.* (2006) and Citro *et al.* (2017) for the sphere. We achieve agreement in St_1 within 0.1% to 1.5% and in the mean drag coefficient C_x within 0.02% to 0.7% , indicating that the present discretisation is sufficiently refined to capture the key features of the wake flow. As also shown in table 5, a sensitivity study revealed that a polynomial order of $N = 7$ is optimal, as higher values of N offered minimal improvements while significantly increasing computational cost.

Cube references	Type	Dom. size (In, Out, Sides)	Re_{c1}	Re_{c2}	St_1	
Saha (2004)	Num	$6D, 22D, \pm 7D$	216	270	0.094 ($Re = 290$)	
Klotz <i>et al.</i> (2014)	Exp	71.66D stream dir., $\pm 4.16D$	186	285	0.125 ($Re_{c2} < Re < 390$)	
Khan <i>et al.</i> (2020b)	Num	$8D, 17D, \pm 7.5D$	200–215	250–276	0.088 ($Re = 276$)	
Meng <i>et al.</i> (2021)	Num	$7.5D, 30D, \pm 7.5D$	207	252	0.0975 ($Re = 270$)	
Sphere references	Type	Dom. size (In, out, sides)	Order	Re_{c1}	Re_{c2}	St_1 at Re_{c2}
Meliga <i>et al.</i> (2009b)	Num	$100D, 200D, \pm 25D$	—	212.6	280.7	0.111
Ghidersa & Dušek (2000)	Num	$12D, 25D, \pm 8D$	$N = 6$	212.0	272.3	0.127
Bouchet <i>et al.</i> (2006)	Num	$12D, 25D, \pm 8D$	$N = 8$	211.9	274	0.128
Szaltys <i>et al.</i> (2012)	Exp	—, —, $\pm 3.125D$	—	212.0	268.0	0.180
Citro <i>et al.</i> (2017)	Num	$10D, 30D, \pm 10D$	$N = 10$	212.8	272.9	0.128
Citro <i>et al.</i> (2017)	Num	$14D, 38D, \pm 14D$	$N = 13$	212.4	271.8	0.129
Sansica <i>et al.</i> (2018)	Num	$10D, 10D, \pm 5D$	—	212.5	275.2	0.118

Table 4. Comparison of domain sizes, critical Reynolds numbers (Re_{c1} , Re_{c2}), and fundamental shedding frequencies (St_1) from various numerical (Num) and experimental (Exp) studies of flow past a cube (top) and a sphere (bottom). For sphere references using a spectral-element method, the polynomial order N is listed where available.

Appendix C. Consistency verification

We verify the consistency of the critical frequencies identified by our linear stability analysis for Hopf (II) and Neimark–Sacker (III) bifurcations by comparing them with the dominant frequencies observed in nonlinear simulations at Reynolds numbers close to these bifurcation points. Specifically, St_1 denotes the primary frequency of the periodic flow that emerges following the secondary bifurcation in the nonlinear simulations, while $St_{c,1}^L$ remains the fundamental frequency predicted by linear stability, interpolated at $Re_{c,2}^L$.

For the tertiary Neimark–Sacker bifurcation, St_1 and St_2 represent two incommensurate frequencies corresponding to (i) the vortex-shedding mode and (ii) the additional secondary frequency that appears once the flow surpasses the tertiary threshold. In parallel, $St_{c,1}^L$ and $St_{c,2}^L$ continue to denote the critical fundamental and secondary frequencies derived from the Floquet analysis, interpolated for $Re_{c,1}^L$ and $Re_{c,2}^L$, respectively.

Table 6 summarises, for both cube and sphere, the comparison between these critical frequencies from linear stability analysis (LSA) presented in this paper and those measured in our nonlinear DNS for the secondary (Hopf) and tertiary (Neimark–Sacker) bifurcations. First, we note that St_1 from the nonlinear simulation, run at a supercritical Reynolds number near $Re_{c,2}^L$, matches closely with $St_{c,1}^L$ from figure 8. For example, at $Re = 251$ for the cube, the DNS yields $St_1 = 0.0930$, while the linear prediction gives $St_{c,1}^L = 0.0927$. Similarly, for the sphere at $Re = 275$, the DNS frequency of $St_1 = 0.1299$ compares well with the linear result of $St_{c,1}^L = 0.1282$.

Furthermore, for both geometries, performing DNS at Reynolds numbers just beyond $Re_{c,3}^L$ (i.e. where the tertiary bifurcation triggers) leads to a new frequency St_2 , which coincides closely with the three-dimensional Floquet prediction $St_{c,2}^L$ (cf. figure 15) (comparison between the values reported in columns ‘ $St_{c,2}^L$ at $Re_{c,3}^L$ ’ and ‘ St_2 ’ of the ‘Tertiary III’ part of table 6). For instance, the cube at $Re = 281$ exhibits $St_2 = 0.0282$ against an LSA prediction of $St_{c,2}^L = 0.0276$, while for the sphere at $Re = 332$, we obtain $St_2 = 0.0393$ compared with a prediction of $St_{c,2}^L = 0.0385$.

Cube at $Re = 270$				
Case	St_1	$\overline{C_x}$	$\overline{C_y}$	$dt \times 10^{-3}$
Meng <i>et al.</i> (2021) (DNS)	0.0975	0.866	—	2.5
Present $N = 5$	0.0974	0.8658	−0.0736	4.6
Present $N = 7$	0.0975	0.8598	−0.0734	2.5
Present $N = 9$	0.0979	0.8587	−0.0733	1.7

Sphere at $Re = 275$				
Case	St_1	$\overline{C_x}$	$\overline{C_y}$	$dt \times 10^{-3}$
Bouchet <i>et al.</i> (2006) (LSA, $N = 8$, N_{elem} in $z-r$ domain = 169)	0.1279	0.678	0.066	—
Citro <i>et al.</i> (2017) (LSA, $N = 10$, $N_{elem} = 8$, 510)	0.1296	—	—	—
Present $N = 5$	0.1281	0.6750	−0.0650	1.4
Present $N = 7$	0.1299	0.6750	−0.0649	0.75
Present $N = 9$	0.1292	0.6749	−0.0648	0.47

Table 5. Comparison of the Strouhal number St_1 , mean drag $\overline{C_x}$, mean lift $\overline{C_y}$, and time step Δt for the cube at $Re = 270$ and the sphere at $Re = 275$, obtained using different polynomial orders N . Present results are averaged over 100 shedding periods (non-dimensional times $T = 1026$ for the cube and $T = 772$ for the sphere). Data from Meng *et al.* (2021) (for the cube) and Bouchet *et al.* (2006) (for the sphere) are interpolated from published curves.

		LSA	DNS
		$St_{c,1}^L$ at $Re_{c,2}^L$	St_1
Secondary II	Cube	0.0927 ($Re_{c,2}^L = 250.61$)	0.0930 ($Re = 251$)
	Sphere	0.1282 ($Re_{c,2}^L = 273.67$)	0.1299 ($Re = 275$)

		Newton–UPO	LSA	DNS	
		$St_{c,1}$ at $Re_{c,3}^L$	$St_{c,2}^L$ at $Re_{c,3}^L$	St_1	St_2
Tertiary III	Cube	0.0980	0.0276 ($Re_{c,3}^L = 280.31$)	0.0975 ($Re = 281$)	0.0282 ($Re = 281$)
	Sphere	0.1353	0.0385 ($Re_{c,3}^L = 330.75$)	0.1333 ($Re = 332$)	0.0393 ($Re = 332$)

Table 6. Comparison of critical frequencies predicted by linear stability analysis (LSA) and measured in nonlinear simulations (DNS) for the secondary (Hopf) and tertiary (Neimark–Sacker) bifurcations. The table lists the fundamental frequency $St_{c,1}^L$ at $Re_{c,2}^L$ for the secondary bifurcation and both $St_{c,1}$ and $St_{c,2}^L$ at $Re_{c,3}^L$ for the tertiary bifurcation. Corresponding DNS values for St_1 and St_2 are shown for cube and sphere cases at nearby supercritical Reynolds numbers.

These new frequencies induce quasiperiodic flow characterised by two incommensurate frequencies, leading to trajectories in phase-space that do not repeat exactly. In addition, the stabilised limit cycle frequencies $St_{c,1}$ at $Re_{c,3}^L$ (denoted ‘Newton–UPO’ in table 6) give the critical fundamental frequency of the orbit as computed by the Newton–GMRES approach (see figure 12). The close agreement between St_1 and $St_{c,1}$ arises because the

DNS is conducted at a Reynolds number very close to $Re_{c,3}$, where the nonlinear distortion of the base flow is low.

Appendix D. Base flow computation

In this section, we expose the present methodology used to compute the steady base flows \mathbf{Q} and the periodic ones $\mathbf{Q}(t)$. We first detail the computation of fixed points and subsequently extend our methodology to the stabilisation of unstable periodic orbits (UPOs). In both cases, base flows are computed using the Jacobian-free Newton–Krylov method, implemented within the open-source NekStab toolbox for Nek5000.

D.1. Fixed points

Fixed points are defined as solutions that satisfy the condition:

$$\mathbf{X} = \Phi_\tau(\mathbf{X}), \quad (\text{D1})$$

where Φ_τ represents the evolution operator (nonlinear solver of (2.1)) over a time interval τ , meaning that they are the roots of the following equation:

$$\mathcal{F}(\mathbf{X}) = \Phi_\tau(\mathbf{X}) - \mathbf{X}. \quad (\text{D2})$$

In the present work, the computation of fixed points is framed within a time-stepping approach. In this method, the state of the system is updated iteratively as

$$\mathbf{X}_{k+1} = \Phi_\tau(\mathbf{X}_k), \quad (\text{D3})$$

where \mathbf{X}_k represents the state vector at iteration k . Analogously, we presume the availability of a linearised variant of this code (linear solver of (2.3)) to advance the linearised state over time:

$$\mathbf{x}_{k+1} = \mathbf{M}_\tau \mathbf{x}_k, \quad (\text{D4})$$

where $\mathbf{M}_\tau = \exp(\tau \mathbf{L})$ is the numerically approximated exponential propagator, with \mathbf{L} the linearised operator around the current approximation \mathbf{X}_k .

To compute fixed points, i.e. solutions verifying (D2), we employ an inexact Newton method (Dembo, Eisenstat & Steihaug 1982) with scheduled tightening of the solver's tolerances. In the Newton–Krylov method, the Jacobian of (D2), denoted as $\mathbf{J} = \mathbf{M}_\tau - \mathbf{I}$, is used to iteratively solve for the corrections \mathbf{x} . The inexact Newton–Krylov method proceeds as follows.

- (i) Compute the residual of the nonlinear equation

$$\mathbf{r}_k = \Phi_\tau(\mathbf{X}_k) - \mathbf{X}_k. \quad (\text{D5})$$

If $\|\mathbf{r}_k\|$ is below a predefined threshold ε , \mathbf{X}_k is accepted as the base flow solution. Otherwise, proceed to the next step.

- (ii) Compute the Newton correction \mathbf{x} by solving the linear system

$$\mathbf{J}\mathbf{x} = -\mathbf{r}_k, \quad (\text{D6})$$

subject to the relaxed solvers tolerances ε . In practice, this involves solving

$$(\exp(\tau \mathbf{L}) - \mathbf{I}) \mathbf{x} = -\mathbf{r}_k. \quad (\text{D7})$$

- (iii) Update the solution using the correction $\mathbf{X}_{k+1} = \mathbf{X}_k + \mathbf{x}$.

D.2. Periodic orbits

The computation of UPOs follows a similar process to that of fixed points, but includes modifications to account for the periodic nature of the solutions.

Periodic orbits satisfy the condition

$$\mathbf{X} = \Phi_\tau(\mathbf{X}) \quad (\text{D8})$$

for a specific period $\tau = \tau^*$, and are solutions to the equation

$$\mathcal{F}(\mathbf{X}, \tau) = \Phi_\tau(\mathbf{X}) - \mathbf{X} = \mathbf{0}. \quad (\text{D9})$$

The unknowns of this system are the state vector \mathbf{X} and the period τ . Since the system has one more unknown than equations, an additional phase condition is introduced to uniquely identify a point in the orbit. This condition, based on an initial guess \mathbf{X}_0 , takes the form:

$$\mathbf{F}(\mathbf{X}_0) \cdot (\mathbf{X} - \mathbf{X}_0) = 0, \quad (\text{D10})$$

where $\mathbf{F}(\mathbf{X}_0)$ is the time derivative of the flow map evaluated at \mathbf{X}_0 .

The state of the system evolves by time-stepping (2.1) as

$$\mathbf{X}_{k+1} = \Phi_\tau(\mathbf{X}_k), \quad (\text{D11})$$

where Φ_τ represents the flow map over a time period τ , and \mathbf{X}_k is the state at time step k . The corresponding linearised system of (2.3) evolves as

$$\mathbf{x}_{k+1} = \mathbf{M}_\tau \mathbf{x}_k, \quad (\text{D12})$$

where $\mathbf{M}_\tau = \int_0^\tau \mathcal{L}(t) dt$ is the monodromy matrix.

The augmented system, combining (D9) and the phase condition (D10) has a Jacobian matrix defined as

$$\mathbf{J} = \begin{pmatrix} \mathbf{M}_\tau - \mathbf{I} & \mathbf{F}(\Phi_\tau(\mathbf{X}_k)) \\ \mathbf{F}^T(\mathbf{X}_k) & 0 \end{pmatrix}, \quad (\text{D13})$$

and is solved using the Newton–Krylov method. The iterative steps include the following.

- (i) Compute the residual $\mathbf{r}_k = \Phi_\tau(\mathbf{X}_k) - \mathbf{X}_k$. If $\|\mathbf{r}_k\|$ is below the threshold ε , \mathbf{X}_k is accepted as the periodic orbit solution. Otherwise, proceed to the next step.
- (ii) Determine the Newton correction $\delta\mathbf{x}$ and $\delta\tau$ by solving the bounded system

$$\begin{pmatrix} \mathbf{M}_\tau - \mathbf{I} & \mathbf{F}(\Phi_\tau(\mathbf{X}_k)) \\ \mathbf{F}^T(\mathbf{X}_k) & 0 \end{pmatrix} \begin{pmatrix} \delta\mathbf{x} \\ \delta\tau \end{pmatrix} = - \begin{pmatrix} \mathbf{r}_k \\ 0 \end{pmatrix}. \quad (\text{D14})$$

- (iii) Update the solution $\begin{pmatrix} \mathbf{X}_{k+1} \\ \tau_{k+1} \end{pmatrix} = \begin{pmatrix} \mathbf{X}_k \\ \tau_k \end{pmatrix} + \begin{pmatrix} \delta\mathbf{x} \\ \delta\tau \end{pmatrix}$.

In step (ii), both the original nonlinear system and the linearised one must be marched forward in time to evaluate the matrix-vector product $\mathbf{M}_\tau \delta\mathbf{x}$. To minimise the computational cost associated with this process, we implemented a pre-computation strategy. Specifically, the tentative orbit $\mathbf{X}_k(t)$ is stored at discrete time steps within the period $t \in [0, \tau_k]$. By doing so, we eliminate the need for repeated time integration during each Newton iteration, reducing the computational burden. This storage strategy is enabled by Nek5000's reduced memory footprint and efficient spectral element implementation. For details on the bounded Newton–Krylov method for UPOs, see Frantz *et al.* (2023).

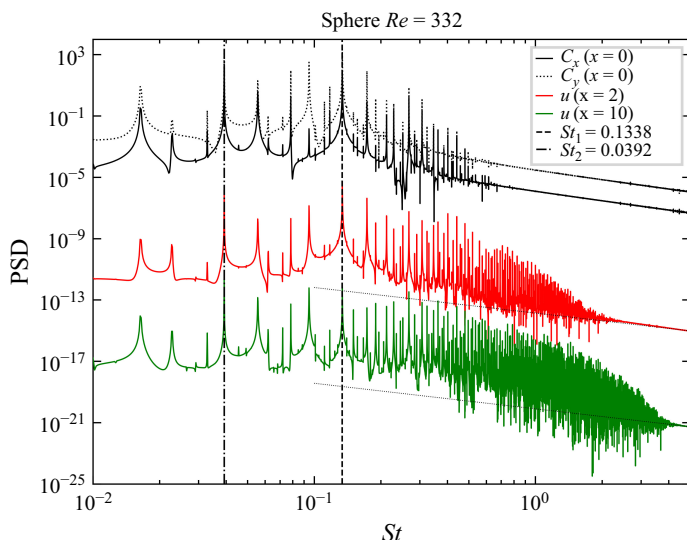


Figure 20. Power spectral density (PSD) for flow past a sphere at $Re = 332$. Comparison between PSD obtained from drag (C_x) and lift (C_y) signals and from velocity fluctuations at two wake probe locations, $(x, y, z) = (2, 0, 0)$ (near the body) and $(x, y, z) = (10, 0, 0)$ (further downstream). The PSD highlights the dominant frequencies St_1 (dashed vertical line) and St_2 (dash-dotted vertical line) associated with vortex shedding and their coupling between body forces and wake dynamics.

Appendix E. Spectral analysis

In this appendix, we examine the spectral characteristics of the flow dynamics and body forces to clarify how forces acting on the body synchronise with the velocity field in its wake. Figure 20 presents, for the sphere at $Re = 332$ (quasiperiodic regime), the power spectral density (PSD) of the drag and lift signals, along with the PSD of the velocity fluctuations measured at two probe locations in the wake: $(x, y, z) = (2, 0, 0)$ (near the body) and $(x, y, z) = (10, 0, 0)$ (further downstream). The PSD results illuminate the dominant frequencies associated with both the body forces and the local velocity field, reflecting the influence of vortex shedding and its interactions with the body. In particular, the spectral peaks align closely among lift, drag and measured velocity fluctuations, indicating a strong coupling mediated by a global instability that governs the wake dynamics. At the upstream probe, the dominant frequency exhibits a higher amplitude, revealing strong velocity fluctuations close to the body. Further downstream, the spectral energy diminishes, yet the coherent frequency content persists. This progression highlights the nonlinear transformations, convection and eventual diffusion of flow structures as they evolve in the wake. The enduring presence of a dominant frequency underscores the stability and persistent influence of the underlying vortex shedding process.

REFERENCES

- ACHENBACH, E. 1974 Vortex shedding from spheres. *J. Fluid Mech.* **62** (2), 209–221.
 AHMED, S.R., RAMM, G. & FALTIN, G. 1984 Some salient features of the time-averaged ground vehicle wake. *SAE Trans.* 473–503.
 ARNOLD, V.I. 2012 *Geometrical Methods in the Theory of Ordinary Differential Equations*. vol. 250, Springer Science & Business Media.
 AUGUSTE, F., FABRE, D. & MAGNAUDET, J. 2010 Bifurcations in the wake of a thick circular disk. *Theor. Comput. Fluid Dyn.* **24** (1), 305–313.
 BARKLEY, D. 2005 Confined three-dimensional stability analysis of the cylinder wake. *Phys. Rev. E* **71** (1), 017301.

- BARKLEY, D. & HENDERSON, R.D. 1996 Three-dimensional Floquet stability analysis of the wake of a circular cylinder. *J. Fluid Mech.* **322**, 215–241.
- BLACKBURN, H.M. & LOPEZ, J.M. 2003 On three-dimensional quasiperiodic Floquet instabilities of two-dimensional bluff body wakes. *Phys. Fluids* **15** (8), L57–L60.
- BLACKBURN, H.M., MARQUES, F. & LOPEZ, J.M. 2005 Symmetry breaking of two-dimensional time-periodic wakes. *J. Fluid Mech.* **522**, 395–411.
- BOBINSKI, T., GOUJON-DURAND, S. & WESFREID, J.E. 2014 Instabilities in the wake of a circular disk. *Phys. Rev. E* **89** (5), 053021.
- BOHORQUEZ, P., SANMIGUEL-ROJAS, E., SEVILLA, A., JIMÉNEZ-GONZÁLEZ, J.I. & MARTÍNEZ-BAZÁN, C. 2011 Stability and dynamics of the laminar wake past a slender blunt-based axisymmetric body. *J. Fluid Mech.* **676**, 110–144.
- BOUCHET, G., MEBAREK, M. & DUŠEK, J. 2006 Hydrodynamic forces acting on a rigid fixed sphere in early transitional regimes. *Eur. J. Mech. B Fluids* **25** (3), 321–336.
- BUCCI, M.A., CHERUBINI, S., LOISEAU, J.-CH & ROBINET, J.-CH 2021 Influence of freestream turbulence on the flow over a wall roughness. *Phys. Rev. Fluids* **6** (6), 063903.
- BUCCI, M.A., PUCKERT, D.K., ANDRIANO, C., LOISEAU, J.-C., CHERUBINI, S., ROBINET, J.-C. & RIST, U. 2018 Roughness-induced transition by quasi-resonance of a varicose global mode. *J. Fluid Mech.* **836**, 167–191.
- CHESTER, W., BREACH, D.R. & PROUDMAN, I. 1969 On the flow past a sphere at low Reynolds number. *J. Fluid Mech.* **37** (4), 751–760.
- CHIARINI, A. & BOUJO, E. 2025 Stability and dynamics of the laminar flow past rectangular prisms. *J. Fluid Mech.* **1008**, A33.
- CHOI, H., LEE, J. & PARK, H. 2014 Aerodynamics of heavy vehicles. *Annu. Rev. Fluid Mech.* **46**, 441–468.
- CHOMAZ, J.M., HUERRE, P. & REDEKOPP, L.G. 1988 Bifurcations to local and global modes in spatially developing flows. *Phys. Rev. Lett.* **60** (1), 25.
- CHRUST, M., GOUJON-DURAND, S. & WESFREID, J.E. 2013 Loss of a fixed plane of symmetry in the wake of a sphere. *J. Fluids Struct.* **41**, 51–56.
- CITRO, V., SICONOLFI, L., FABRE, D., GIANNETTI, F. & LUCHINI, P. 2017 Stability and sensitivity analysis of the secondary instability in the sphere wake. *AIAA J.* **55** (11), 3661–3668.
- COHEN, J., KARP, M. & MEHTA, V. 2014 A minimal flow-elements model for the generation of packets of hairpin vortices in shear flows. *J. Fluid Mech.* **747**, 30–43.
- CONSTANTINESCU, G. & SQUIRES, K. 2004 Numerical investigations of flow over a sphere in the subcritical and supercritical regimes. *Phys. Fluids* **16** (5), 1449–1466.
- DEMBO, R.S., EISENSTAT, S.C. & STEIHAUG, T. 1982 Inexact newton methods. *SIAM J. Numer. Anal.* **19** (2), 400–408.
- DONG, X., GAO, Y. & LIU, C. 2019 New normalized vortex/vortex identification method. *Phys. Fluids* **31** (1), 011701.
- FABRE, D., AUGUSTE, F. & MAGNAUDET, J. 2008 Bifurcations and symmetry breaking in the wake of axisymmetric bodies. *Phys. Fluids* **20** (5), 051702.
- FERNANDES, P.C., RISSO, F., ERN, P. & MAGNAUDET, J. 2007 Oscillatory motion and wake instability of freely rising axisymmetric bodies. *J. Fluid Mech.* **573**, 479–502.
- FISCHER, P., KRUSE, J., MULLEN, J., TUFO, H., LOTTES, J. & KERKEMEIER, S. 2008 *Nek5000: open source spectral element CFD solver*. Argonne National Laboratory, Mathematics and Computer Science Division.
- FISCHER, P. & MULLEN, J. 2001 Filter-based stabilization of spectral element methods. *Comptes Rendus De l'Académie Des Sciences-Series I-Mathematics* **332** (3), 265–270.
- FISCHER, P.F. 1997 An overlapping Schwarz method for spectral element solution of the incompressible Navier–Stokes equations. *J. Comput. Phys.* **133** (1), 84–101.
- FRANTZ, R.A.S., LOISEAU, J.-C. & ROBINET, J.-C. 2023 Krylov methods for large-scale dynamical systems: application in fluid dynamics. *ASME. Appl. Mech. Rev.* **75** (3), 030802.
- FRANTZ, R.S. 2022 Instabilités et transition à la turbulence dans les écoulements périodiques PhD thesis, HESAM Université, France.
- GENNARO, E.M., COLACITI, A.K. & MEDEIROS, M.A.F. 2013 On the controversy regarding the effect of flow shear on the Strouhal number of cylinder vortex shedding. *Aerosp. Sci. Technol.* **29** (1), 313–320.
- GHIDERSA, B. & DUŠEK, J.A.N. 2000 Breaking of axisymmetry and onset of unsteadiness in the wake of a sphere. *J. Fluid Mech.* **423**, 33–69.
- GIANNETTI, F., CAMARRI, S. & LUCHINI, P. 2010 Structural sensitivity of the secondary instability in the wake of a circular cylinder. *J. Fluid Mech.* **651**, 319–337.
- GOLDBURG, A. & FLORSHEIM, B.H. 1966 Transition and strouhal number for the incompressible wake of various bodies. *Phys. Fluids* **9** (1), 45–50.

- GRANDEMANGE, M., CADOT, O. & GOHLKE, M. 2012 Reflectional symmetry breaking of the separated flow over three-dimensional bluff bodies. *Phys. Rev. E* **86** (3), 035302.
- GUMOWSKI, K., MIEDZIK, J., GOUJON-DURAND, S., JENFFER, P. & WESFREID, J.E. 2008 Transition to a time-dependent state of fluid flow in the wake of a sphere. *Phys. Rev. E* **77** (5), 055308.
- HENDERSON, R.D. & BARKLEY, D. 1996 Secondary instability in the wake of a circular cylinder. *Phys. Fluids* **8** (6), 1683–1685.
- JACKSON, C.P. 1987 A finite-element study of the onset of vortex shedding in flow past variously shaped bodies. *J. Fluid Mech.* **182**, 23–45.
- JOHNSON, T.A. & PATEL, V.C. 1999 Flow past a sphere up to a Reynolds number of 300. *J. Fluid Mech.* **378**, 19–70.
- KALRO, V. & TEZDUYAR, T. 1998 3D computation of unsteady flow past a sphere with a parallel finite element method. *Comput. Meth. Appl. Mech. Engng* **151** (1–2), 267–276.
- KARNIADAKIS, G.E. & TRIANTAFYLLOU, G.S. 1992 Three-dimensional dynamics and transition to turbulence in the wake of bluff objects. *J. Fluid Mech.* **238**, 1–30.
- KELKAR, K.M. & PATANKAR, S.V. 1992 Numerical prediction of vortex shedding behind a square cylinder. *Intl J. Numer. Meth. Fluids* **14** (3), 327–341.
- KHAN, M.H., KHAN, H.H., SHARMA, A. & AGRAWAL, A. 2020a Laminar vortex shedding in the wake of a cube. *J. Fluids Engng* **142** (11), 111301.
- KHAN, M.H., SHARMA, A. & AGRAWAL, A. 2020b Simulation of flow around a cube at moderate Reynolds numbers using the lattice Boltzmann method. *J. Fluids Engng* **142** (1), 011301.
- KIM, D. & CHOI, H. 2002 Laminar flow past a sphere rotating in the streamwise direction. *J. Fluid Mech.* **461**, 365–386.
- KIM, D. & CHOI, H. 2003 Laminar flow past a hemisphere. *Phys. Fluids* **15** (8), 2457–2460.
- KIYA, M., ISHIKAWA, H. & SAKAMOTO, H. 2001 Near-wake instabilities and vortex structures of three-dimensional bluff bodies: a review. *J. Wind Engng Ind. Aerodyn.* **89** (14–15), 1219–1232.
- KLOTZ, L., GOUJON-DURAND, S., ROKICKI, J. & WESFREID, J.E. 2014 Experimental investigation of flow behind a cube for moderate Reynolds numbers. *J. Fluid Mech.* **750**, 73–98.
- KUMAR, B. & MITTAL, S. 2006 Effect of blockage on critical parameters for flow past a circular cylinder. *Intl J. Numer. Meth. Fluids* **50** (8), 987–1001.
- LEE, S. 2000 A numerical study of the unsteady wake behind a sphere in a uniform flow at moderate Reynolds numbers. *Comput. Fluids* **29** (6), 639–667.
- LOISEAU, J.-CH, BUCCI, M.A., CHERUBINI, S. & ROBINET, J.-CH 2019 Time-stepping and Krylov methods for large-scale instability problems. In *Computational Modelling of Bifurcations and Instabilities in Fluid Dynamics*, pp. 33–73. Springer.
- LOISEAU, J.-CH, ROBINET, J.-CH, CHERUBINI, S. & LERICHE, E. 2014 Investigation of the roughness-induced transition: global stability analyses and direct numerical simulations. *J. Fluid Mech.* **760**, 175–211.
- MAGARVEY, R.H. & BISHOP, R.L. 1961 Wakes in liquid-liquid systems. *Phys. Fluids* **4** (7), 800–805.
- MARQUET, O. & LARSSON, M. 2015 Global wake instabilities of low aspect-ratio flat-plates. *Eur. J. Mech. B Fluids* **49**, 400–412.
- MELIGA, P., CHOMAZ, J.-M. & SIPP, D. 2009a Global mode interaction and pattern selection in the wake of a disk: a weakly nonlinear expansion. *J. Fluid Mech.* **633**, 159–189.
- MELIGA, P., CHOMAZ, J.-M. & SIPP, D. 2009b Unsteadiness in the wake of disks and spheres: instability, receptivity and control using direct and adjoint global stability analyses. *J. Fluids Struct.* **25** (4), 601–616.
- MENG, Q., AN, H., CHENG, L. & KIMIAEI, M. 2021 Wake transitions behind a cube at low and moderate Reynolds numbers. *J. Fluid Mech.* **919**, A44.
- MITTAL, R. 1999 Planar symmetry in the unsteady wake of a sphere. *AIAA J.* **37** (3), 388–390.
- MITTAL, R. & NAJJAR, F. 1999 Vortex dynamics in the sphere wake. In *30th Fluid Dynamics Conference*, pp. 3806. AIAA.
- NAKAMURA, I. 1976 Steady wake behind a sphere. *Phys. Fluids* **19** (1), 5–8.
- NATARAJAN, R. & ACRIVOS, A. 1993 The instability of the steady flow past spheres and disks. *J. Fluid Mech.* **254**, 323–344.
- NEIMARK, J. 1959 On some cases of periodic motions depending on parameters. *Dokl. Akad. Nauk SSSR* **129**, 736–739.
- ORSZAG, S.A. 1971 On the elimination of aliasing in finite-difference schemes by filtering high-wavenumber components. *J. Atmos. Sci.* **28** (6), 1074–1074.
- PICELLA, F., LOISEAU, J.-CH, LUSSEYRAN, F., ROBINET, J.-CH, CHERUBINI, S. & PASTUR, L. 2018 Successive bifurcations in a fully three-dimensional open cavity flow. *J. Fluid Mech.* **844**, 855–877.
- PIER, B. 2008 Local and global instabilities in the wake of a sphere. *J. Fluid Mech.* **603**, 39–61.

- PIERSON, J.-L., AUGUSTE, F., HAMMOUTI, A. & WACHS, A. 2019 Inertial flow past a finite-length axisymmetric cylinder of aspect ratio 3: effect of the yaw angle. *Phys. Rev. Fluids* **4** (4), 044802.
- PROVANSAL, M., MATHIS, C. & BOYER, L. 1987 Bénard-von Kármán instability: transient and forced regimes. *J. Fluid Mech.* **182**, 1–22.
- RICHTER, A. & NIKRITYUK, P.A. 2012 Drag forces and heat transfer coefficients for spherical, cuboidal and ellipsoidal particles in cross flow at sub-critical Reynolds numbers. *Intl J. Heat Mass Transfer* **55** (4), 1343–1354.
- RIGAS, G., ESCLAPEZ, L. & MAGRI, L. 2017 Symmetry breaking in a 3D bluff-body wake, arXiv preprint arXiv: 1703.07405.
- ROBICHAUX, J., BALACHANDAR, S. & VANKA, S.P. 1999 Three-dimensional Floquet instability of the wake of square cylinder. *Phys. Fluids* **11** (3), 560–578.
- SACKER, R.J. 1964 *On Invariant Surfaces and Bifurcation of Periodic Solutions of Ordinary Differential Equations*. New York University.
- SAHA, A.K. 2004 Three-dimensional numerical simulations of the transition of flow past a cube. *Phys. Fluids* **16** (5), 1630–1646.
- SAHA, A.K. 2006 Three-dimensional numerical study of flow and heat transfer from a cube placed in a uniform flow. *Intl J. Heat Fluid Flow* **27** (1), 80–94.
- SAKAMOTO, H. & HANIU, H. 1990 A study on vortex shedding from spheres in a uniform flow. *J. Fluids Engng* **112** (4), 386–392.
- SAKAMOTO, H. & HANIU, H. 1995 The formation mechanism and shedding frequency of vortices from a sphere in uniform shear flow. *J. Fluid Mech.* **287**, 151–171.
- SANO, T. 1981 Unsteady flow past a sphere at low Reynolds number. *J. Fluid Mech.* **112**, 433–441.
- SANSICA, A., OHMICH, Y., ROBINET, J.-CH & HASHIMOTO, A. 2020 Laminar supersonic sphere wake unstable bifurcations. *Phys. Fluids* **32** (12), 126107.
- SANSICA, A., ROBINET, J.-CH, ALIZARD, F. & GONCALVES, E. 2018 Three-dimensional instability of a flow past a sphere: Mach evolution of the regular and Hopf bifurcations. *J. Fluid Mech.* **855**, 1088–1115.
- SCHOUVEILER, L. & PROVANSAL, M. 2002 Self-sustained oscillations in the wake of a sphere. *Phys. Fluids* **14** (11), 3846–3854.
- SHEARD, G.J., THOMPSON, M.C. & HOURIGAN, K. 2003 From spheres to circular cylinders: the stability and flow structures of bluff ring wakes. *J. Fluid Mech.* **492**, 147–180.
- SHENOY, A.R. & KLEINSTREUER, C. 2008 Flow over a thin circular disk at low to moderate Reynolds numbers. *J. Fluid Mech.* **605**, 253–262.
- SIERRA-AUSÍN, J., LORITE-DÍEZ, M., JIMÉNEZ-GONZÁLEZ, J.I., CITRO, V. & FABRE, D. 2022 Unveiling the competitive role of global modes in the pattern formation of rotating sphere flows. *J. Fluid Mech.* **942**, A54.
- SOHANKAR, A., NORBERG, C. & DAVIDSON, L. 1998 Low-Reynolds-number flow around a square cylinder at incidence: study of blockage, onset of vortex shedding and outlet boundary condition. *Intl J. Numer. Meth. Fluids* **26** (1), 39–56.
- STEWART, G.W. 2001 A Krylov–Schur algorithm for large eigenproblems. *SIAM J. Matrix Anal. Appl.* **23**, 601–614.
- SZALTYS, P., CHRUST, M., PRZADKA, A., GOIJON-DURAND, S., TUCKERMAN, L.S. & WESFREID, J.E. 2012 Nonlinear evolution of instabilities behind spheres and disks. *J. Fluids Struct.* **28**, 483–487.
- TANEDA, S. 1956 Experimental investigation of the wake behind a sphere at low Reynolds numbers. *J. Phys. Soc. Jpn.* **11** (10), 1104–1108.
- THOMPSON, M.C., LEWEKE, T. & PROVANSAL, M. 2001 Kinematics and dynamics of sphere wake transition. *J. Fluids Struct.* **15** (3–4), 575–585.
- TOMBOULIDES, A., ORSZAG, S. & KARNIADAKIS, G. 1993 Direct and large-eddy simulations of axisymmetric wakes. In *31st Aerospace Sciences Meeting*, pp. 546. AIAA.
- TOMBOULIDES, A.G. & ORSZAG, S.A. 2000 Numerical investigation of transitional and weak turbulent flow past a sphere. *J. Fluid Mech.* **416**, 45–73.
- TORLAK, M., HALAČ, A., ALISPAHIĆ, M. & HADŽIABDIĆ, V. 2019 Computation of the fluid flow around polyhedral bodies at low reynolds numbers. In *International Symposium on Innovative and Interdisciplinary Applications of Advanced Technologies*, pp. 324–333. Springer.
- YAGINUMA, T. & ITO, H. 2008 Drag and wakes of freely falling 60° cones at intermediate Reynolds numbers. *Phys. Fluids* **20** (11), 117102.
- YANG, Y., FENG, Z. & ZHANG, M. 2022 Onset of vortex shedding around a short cylinder. *J. Fluid Mech.* **933**, A7.